Accepted Manuscript

Cellulose acetate/AgNPs-organoclay and/or thymol nano-biocomposite films with combined antimicrobial/antioxidant properties for active food packaging use

Nassima Dairi, Hafida Ferfera-Harrar, Marina Ramos, María Carmen Garrigós

PII: S0141-8130(18)33172-6
DOI: doi:10.1016/j.ijbiomac.2018.10.042
Reference: BIOMAC 10693

To appear in: *International Journal of Biological Macromolecules*

Received date: 26 June 2018
Revised date: 10 September 2018
Accepted date: 10 October 2018

Please cite this article as: Nassima Dairi, Hafida Ferfera-Harrar, Marina Ramos, María Carmen Garrigós , Cellulose acetate/AgNPs-organoclay and/or thymol nano-biocomposite films with combined antimicrobial/antioxidant properties for active food packaging use. Biomac (2018), doi:10.1016/j.ijbiomac.2018.10.042

Cellulose acetate/AgNPs-organoclay and/or thymol nano-biocomposite films with combined antimicrobial/antioxidant properties for active food packaging use

Nassima Dairi[a], Hafida Ferfera-Harrar[a]*, Marina Ramos[b], María Carmen Garrigós[b]

[a] Materials Polymer Laboratory, Department of Macromolecular Chemistry, Faculty of Chemistry, University of Sciences and Technology Houari Boumediene USTHB, B.P. 32 El-Alia, 16111 Algiers, Algeria

[b] Analytical Chemistry, Nutrition & Food Sciences Department, University of Alicante, P.O. Box 99, E-03080 Alicante, Spain

∗ Corresponding author.

E-mail address: harrarhafida@yahoo.fr (H. Ferfera-Harrar)

Abstract. Nano-biocomposite films based on plasticized cellulose acetate/triethyl citrate (CA/TEC) were prepared with silver nanoparticles (AgNPs)/gelatin-modified montmorillonite nanofiller (AgM) and thymol (Th). AgNPs were biosynthesized *in situ* the clay using *Curcuma longa* (*C. longa)* tuber extract. Full characterization of clay and the formulated films was conducted including morphological, physical and functional properties. From the results, the AgNPs showed spherical shape, face centred cubic crystalline structure, and small average size with narrow distribution. Intercalated structure of films was achieved with some exfoliated platelets and clay aggregates. The glass transition temperature (Tg) of CA increased slightly by the added clay but decreased by Th due to its plasticizing effect. Also, the thermal stability of CA was enhanced only by the added clay. Increasing contents of both additives into films declined the optical clarity but enhanced greatly the UV barrier ability. The clay improved the tensile and oxygen barrier properties, while the Th initiated an antagonist effect. Besides, the radical 2,2-diphenyl-1-picrylhydrazyl (DPPH) tests highlighted antioxidant activities of Th-included films. The films showed antimicrobial activities against bacteria and fungi, where *Escherichia Coli* (*E. Coli*) was the most sensitive, with an efficient growth inhibition in vapour-phase method. These materials with antimicrobial/antioxidant properties are promising active packaging.

Keywords. Active food packaging, Cellulose acetate, Silver nanoparticles, Montmorillonite, *Curcuma longa* extract, Thymol, Antimicrobial and antioxidant activities.

1. Introduction

Nano-biocomposites based on biopolymers have been recognized as promising technologies toward their innovative application in eco-friendly food packaging. In this approach, the use biopolymers as matrix and nanoscale reinforcements as fillers are potential materials developed to overcome some drawbacks of biopolymers, such as insufficient mechanical and barrier performances against water vapour and oxygen, since these are factors with advert influence in food quality and shelf-life. The use of versatile biopolymers such as polyesters, polysaccharides, proteins and lipids, among others, is currently improving to satisfy industrial requirements and consumer desires by maintaining food safety, and minimizing their environmental impact [1-3].

Various types of nanoparticles such as clays and nanometals or metal oxides have been used to prepare nano-biocomposites. Among them, layered silicates such as montmorillonites (natural or organically modified), and kaolinite have attracted great attention for packaging [4-6]. However, challenges remain in increasing the compatibility between clay and polymer matrix and reaching complete dispersion of nanoparticles.

Traditional food packaging materials have passive action in relation to food, since they merely serve to isolate foods from the environment, and do not ensure the required food quality to permit an adequate foods commercialization [7]. However, active packaging complement the traditional packaging with new features that make it possible to optimize the conditions inside the packaging of a food product, thus extending its durability. Packaging with antimicrobial and/or antioxidant properties is becoming an emerging food technology to improve fresh foods stability and potentially offer safety of certain foods products. Current trends include the incorporation of various types of active agents into polymeric materials such as antimicrobials, antioxidants, and flavours, which expand the functionality of the packaging by adding novel or extra functions [8]. Since microbial contamination is primarily a surface phenomenon, the incorporation of antimicrobials additives to polymer films has many advantages due to their high exposure areas.

Silver nanoparticles (AgNPs) are arch inorganic products from the nanotechnology field that have gained boundless interests in packaging applications thanks to their unique properties, such as large surface areas, high thermal stability, and antimicrobial activity. In this context, the incorporation of AgNPs into films packaging as an efficient antimicrobial agent to prevent microbial proliferation on food contact surfaces has emerged [9]. However, there is a need to develop a variety of high-yield and low cost green routes for the synthesis of silver nanoparticles.

In this way, the biogenic synthesis of AgNPs mediated by plants has gained widespread interest as safer alternative to common methods, namely chemical, microbial, and physical (UV irradiation, microwave processing, thermal decomposition, electrolysis, ect) processes. This eco-friendly process is beneficial due to its cost effectiveness, non-pathogenic and easily scaled up for large-scale synthesis. Also, there is no need to use high temperature, pressure, energy and toxic chemicals for production. In this context, numerous reports have been published [10-12] concerning the biosynthesis of AgNPs using extracts of different plant parts such as root, stem, bark, leaf, fruit, flowers, and latex as natural resources. Phytocompounds in the plant extracts serve generally as reducing and capping agents in the reaction with silver nitrate ($AgNO_3$), a commonly used precursor in silver nanoparticles synthesis. This dual action is originated from the combined effects of biomolecules such as proteins, amino acids, carbohydrates, flavonoids, alkaloids, tannins, polyphenols and terpenoids.

Curcuma longa (*C. longa*), a perennial member of the Zingiberaceae family, has been widely used as herbal medicine in many Asian countries for thousands of years. The *C. longa* tuber powder aqueous extract was found to be effective in biosynthesis of AgNPs with various sizes depending on the dose of *C. longa extract* [13- 16].

Besides, AgNPs have a tendency to agglomerate when used alone. To overcome this inconvenient, many researches have used carriers such as clays, in which nanoparticles are supported within inter-lamellar spaces and/or on its external layers surfaces. The AgNPs-loaded clays are renowned to have long-term antimicrobial effects [17].

The effectiveness of the antimicrobial packaging films is guaranteed by a slow migration of the active additives from the films to the surface of the packed product. In nano-biocomposite films, the layered silicate as nanofiller could control of the active agents release [18,19].

To meet consumer demands for more natural products in food active packaging, plant extracts essential oils (EOs), as rich sources of biological active antimicrobial and/or antioxidants compounds, such as thymol (Th), cinnamaldehyde (Ci), eugenol, and carvacrol (CV), have been incorporated into packaging materials to protect sensitive oxidation of food. Thymol, one of the major compounds present in thyme and oregano EOs, has been added to polymer matrices to enhance their antimicrobial and antioxidant performance, and thus increasing biosafety of the packed food [20-23].

Polysaccharides have been used as matrices for biodegradable films packaging. Among them, cellulose acetate (CA) is a cellulosic ester derivative from the most abundant renewable cellulosic raw materials such as cotton, wood and sugarcane. It is widely used in a variety of consumer products owing to its excellent optical clarity and stiffness, films forming at low temperatures and high resistance against heat and chemicals. CA-based films were used in efficient antimicrobial packaging technology and the obtained results revealed featuring capable of inhibiting the growth of pathogenic microorganisms [24,25]. Nonetheless, CA has its own weakness such as stiffness, low dimensional stability under high temperature, and it needs to be plasticized, usually by eco-friendly triethyl citrate (TEC), for being industrially melt processed. The common approach for plastic devices and packing films and coatings applications is to develop nano-biocomposites.

Although there are some reports based on CA/clay nanocomposite films [26-31], studies on their actives nanocomposites provided with antioxidant and/or antimicrobials properties are still limited. For instance, Rodriguez et al. [32] elaborated CA/TEC/Cloisite30B nanocomposites in presence of Th or Ci to evaluate the effects of these actives agents on the physical and the antimicrobial properties of the CA-based films. Pola et al. [33] prepared antimicrobial CA films by incorporating

oregano EO and organophilic clay and highlighted their potential use for postharvest preservation purposes.

The current work is oriented to develop active CA-based nano-biocomposite films to enhance not only the physical and mechanical properties but also to introduce extra antimicrobial and antioxidant properties. First, we realized the biogenic synthesis of AgNPs into gelatin-modified MMt using *C. longa* tuber aqueous extract. Then, the obtained organoclay was added alone or with thymol into plasticized CA films. A full characterization of the formulated films was realized, including morphological and physical properties (thermal, mechanical, optical, oxygen barrier) by several techniques (XRD, TEM, SEM-EDX, UV/Vis, DSC, TGA, mechanical and gas barrier testing) as well as the functional antimicrobial/antioxidant activities. The results were discussed with particular emphasis toward the synergic effects of AgM and Th on the properties of the CA-based films. To our knowledge, the elaboration of these nanomaterials based on wholly renewable resources has not been reported yet.

2. Materials and methods

2.1. Materials

Cellulose acetate (CA, 39.8 wt. % of acetyl content, Mn ca. = 30 000 $g.mol^{-1}$, DS = 2.45) was supplied by Sigma–Aldrich. Gelatin (Ge, type B extracted from bovine skin, isoelectric point (IEP) of 5.05) was purchased from Merck Darmstadt. Triethyl citrate (TEC, 99 % purity) and thymol (Th, 99.5 %) were provided by SAFC Inc and Sigma–Aldrich, respectively. Silver nitrate ($AgNO_3$, ≥ 99 %), 2,2-diphenyl-1-picrylhydrazyl (DPPH, 95%), and solvents of analytical grade (acetone, ethanol, nitric acid) were purchased from Sigma–Aldrich and used without further purification. C. *longa* tubers were purchased from a local market. The montmorillonite (MMt, size fraction < 2μm)

extracted from the bentonite category from Maghnia Roussel was kindly supplied by ENOF Chemical Ltd, Research Company, Algeria. MMt was homoionized with sodium cations (Na^+MMt) and its cation exchange capacity was determined to be about 86.16 mequiv/100 g by conductometric titration [26]. All aqueous solutions were prepared with doubly distilled water (DDW).

2.2. Preparation of AgNPs/Ge-modified MMt (AgM)

2.2.1. Preparation of aqueous C. longa tuber extract

The *Curcuma longa* tubers were thoroughly washed with distilled water to remove the dust and other possible adhering impurities, and they were dried successively at room temperature for 24 h at 60 °C in a hot air oven for 1 h to remove moisture. The tubers were powdered in a mixer, and then 20 g of *C. longa* tuber powder was suspended in 400 mL of DDW and kept under magnetic stirring for 4 h at room temperature followed by fast boiling for 5 min. After cooling, the aqueous extracted from *C. longa* was filtered using Whatman No. 1 filter and then it was stored at 4°C for further use.

2.2.2. Biogenic synthesis of AgNPs into organoclay

Focusing on the use of biomass for biogenic synthesis of silver nanoparticles, in this experiment AgNPs were formed *in situ* the Ge-modified MMt organoclay (**OM)**, as solid support (template), at room temperature using *C. longa* aqueous extract. Firstly, the OM was prepared according to a procedure reported previously [26]. Briefly, Ge powder (1g) was soaked in 50 mL of DDW, heated at 70 °C, and followed by the addition of HCl solution (0.5 M) to adjust the solution pH below IEP of gelatin at pH4. This solution was then added dropwise into a 2 wt. % ultrasonically pretreated Na^+M suspension under vigorous stirring at 70 °C for 2 h. the obtained OM was collected by centrifugation, purified by washing with hot DDW, and dried in an oven at 60 °C.

Next, aqueous suspension of OM sample (50 g L^{-1}) was vigorously stirred for 1 h and then underwent an ultrasonic treatment (Elmasonic bath S60H, 50 Hz) for 30 min. Following, 50 mL of $AgNO_3$ precursor solution (40 mM) was added to the suspension for 24 h. Subsequently, *C. longa* extract (60 mL) was mixed with Ag^+ ions-loaded OM suspension under stirring, and then incubated overnight under dark conditions to avoid any photochemical reactions. The obtained clay, denoted **AgM**, was washed repeatedly with DDW until no residual Ag^+ was detected in the supernatant solution (sodium chloride aqueous solution test), and finally dried overnight in an oven at 80 °C.

2.2.3. Nano-biocomposite films preparation

Plasticized CA nano-biocomposite films were prepared at room temperature by solvent casting method. CA powder (1g) was dissolved in 75 mL of acetone under vigorous magnetic stirring for 1 h and then mixed with 20 wt. % of TEC (with respect to CA). The additive Th was incorporated into some CA/TEC film-forming solution at appropriate contents. Concurrently, a required amount of AgM was dispersed in 25 mL of acetone for 4 h, and then sonicated for 30 min. Next, this suspension was added dropwise to CA solution under vigorous stirring and the mixture was allowed for further 4 h and then sonicated for 30 min. Finally, the mixture was casted on a Petri disk and dried at 40 °C in an oven. Plasticized CA film (pC) without any additives as control, as well as unplasticized CA (npC) were also prepared similarly. Table 1 regroups the experimental conditions of film formulations.

In summary, the films were labelled according to AgM and/or Th additives contents in wt. % with respect to the CA matrix. CA nano-biocomposite films comprising only AgM were denoted pC/AgM**x**, **x** designed 3 or 5 wt. % of clay loading. The formulations obtained with a fixed 5 wt.% of clay content in presence of Th were denoted pC/AgM5/Th**z**, **z** designed 4 or 8 wt.% of Th concentrations level. CA films including only Th agent were denoted pC/Th**z**,

2.3. Characterization

2.3.1. Structural and morphological analysis

Film thickness was measured at ten randomly selected locations over each film surface to the nearest of 0.001 mm using a digital micrometre model 293 MDC-Lite (Mituto, Tokyo, Japan) and the averaged values were used subsequently in calculations.

The UV/Visible diffuse reflectance spectra of powder clays and films were recorded in the range of 200 – 800 nm on UV/Vis SPECORD 200 PLUS analytic Jena spectrometer (Saint-Aubin, France) equipped with an integrating sphere reflectance accessory. The film samples were cut into rectangular pieces and were directly attached to the compartment sample of instrument.

The optical measurements of the films were also carried out from the diffused reflectance spectra. The UV barrier property and transparency were evaluated by measuring light transmittance (T %) in UV and visible regions at 300 nm and 660 nm, respectively. The transparency T_{660}, is defined as opaque (< 30 %), semi-translucent (31-45 %), translucent (46 -75 %) and optically clear (>75 %) [19].

Wide angle X-ray scattering (WAXS) analysis was performed on a BRUKER D8 ADVANCE diffractometer (Madison, WI, USA) at 40 kV using CuKα radiation (λ = 1.5406 Å). The WAXS patterns of clays and films samples were scanned over low angles range 2θ = 1.5 - 10° (0.015° step size, 4 s $step^{-1}$) to determine the interlayer distance (d-spacing) and the clay dispersion. The wide angles range 2θ = 10 - 80° (0.05° step size, 8 s $step^{-1}$) was used to check the presence of AgNPs into clay and to gather information on structural alterations of CA into nano-hybrids films.

Field Emission Scanning Electron Microscopy (FESEM) analysis was conducted to observe the clays surface by using FESEM brand SUPRA 25-ZEISS model (Jena, Germany). The elemental maps were determined using the coupled Energy-Dispersive X-ray micro-analyzer EDX BRUKER brand MERLIN model Quantax 400. Triplicate experiments for each sample were taken.

Inductively Coupled Plasma spectroscopy with Mass Spectrometry detection (ICP-MS) was performed on 7700x Agilent model (Santa Clara, CA, USA) in argon (0.35 L min^{-1}) to quantify the silver and residual sodium elements. Clay sample was treated by nitric acid solution (15 %, v/v) at 80 °C for 2 h and the clear supernatant obtained after removal of solids was subjected to analysis.

Transmission Electron Microscopy (TEM) analysis was realize to evaluate the size distribution of AgNPs as well as the morphology of nanocomposites. TEM micrographs were observed on JEOL Transmission Electron Microscope JEM-2010Plus (Tokyo, Japan) with accelerating voltage 200 kV. The sizes of 100 nanoparticles were measured from TEM images using Image J software. Prior to analysis, films were ultra-microtomed (RMC, model MTXL) to obtain slices of 100 nm thick.

2.3.2. Thermal analysis

Differential scanning calorimetry (DSC) tests of films were conducted using a TA DSC Q-2000 instrument (New Castle, DE, USA) under nitrogen atmosphere (50 mL min^{-1}) at 10 °C min^{-1}. Samples were heated from 25 to 160 °C (3 min hold), cooled to 25 °C (3 min hold), then heated to 240 °C.

The thermal parameters, namely T_g and T_m temperatures and melting enthalpy (ΔH_m), were determined from were obtained from the second scan to discard the effect of thermal history. Crystallinity degree (χ) of each film was calculated from Eq. (1).

$$\chi\,(\%) = \frac{\Delta H_m}{w\,\Delta H_m^{\circ}} \times 100 \quad (1)$$

where ΔH_m (J g^{-1}) is the melting enthalpy of the analysed sample, w is the CA weight fraction in the sample, and $\Delta H°_m$ is the respective value of melting enthalpy for crystalline (100 %) sample. The $\Delta H°_m$ value taken in this work was 58.8 J g^{-1} as proposed by Cerqueira et al. [34].

Thermogravimetric analysis (TGA) of clays and films were recorded on TGA/SDTA 851 METTLER TOLEDO thermal analyzer (Schwarzenbach, Switzerland). Samples were heated from 30 °C to 700 °C at 10 °C min^{-1} under nitrogen flux (50 mL min^{-1}). For clays samples, an oxidative analysis was continued from 700 to 1000 °C under N_2/O_2 air atmosphere.

2.3.3. Mechanical testing

The mechanical properties of films were determined by tensile experiments on ZWICK/ROELL Z010 machine (Ars laquenexy METZ, France) equipped with 2 kN load cell. The tensile parameters, namely tensile strength, elastic Young's modulus and elongation at break (%), were evaluated from stress–strain curves according to ASTM D882-09 standard procedure. All samples were conditioned at 25 °C and 50 % RH for 48 h. Tests were performed with 100 x 10 mm^2 rectangular probes and initial grip separation of 50 mm. Specimens were stretched at 25 mm min^{-1} until breaking. The results were an average of five measurements (± standard deviation).

2.3.4. Oxygen transmission rate tests measurements

The oxygen transmission rate (OTR) tests were conducted on an oxygen permeation analyser SYSTECH Instruments-Model 8500 (Metrotec S.A, Spain). Before testing, films were cut into 14 cm diameter circles, clamped in the diffusion chamber, then equilibrated at 25 ºC and 50 % RH for 24 h.

Tests were taken in triplicate and the mean values of OTR per film thickness were reported as normalized (nOTR) ± standard deviations.

2.3.5. Antioxidant activity tests

The antioxidant activity of films containing thymol was estimated using the stable radical DPPH method according to Byun et al. [35] with some modifications. The DPPH scavenging ability was tested in three simulants, namely 95 % ethanol, 10 % ethanol and 3 % acetic acid. 2 mL of an aliquot of each simulant extract was added to 1 mL of DPPH ethanolic solution (0.1 mM) in a capped tube. The mixture was shaken at room temperature for 60 min in darkness. Next, the decrease in absorbance upon the DPPH reduction was measured at 517 nm on JENWAY 6305 UV/Vis Spectrophotometer (Chelmsford Essex, UK). The antioxidant activity kinetic was also studied in 95 % ethanol as fatty food simulant. In this assay, the extract volume was reduced with respect to DPPH (extract/DPPH: 1/1). Similar tests were conducted with Th and ascorbic acid (As. A), as strong antioxidants agents. All analyses were performed in triplicate. The DPPH scavenging efficiency (%) was calculated from the absorbance of the sample (A_{sample}) with respect to DPPH as control (A_{DPPH}), as given by Eq. (2).

$$\text{DPPH scavenging efficiency (\%)} = \frac{(A_{DPPH} - A_{Sample})}{A_{DPPH}} \times 100 \quad (2)$$

2.3.6. Antimicrobial activity tests

The antimicrobial properties of clays and CA films were tested against food microorganisms (bacteria and fungi). The bacteria applied as models were Gram-negative, namely *Escherichia Coli* (*E. Coli*, ATCC 25922), *Pseudomonas aeruginosa* (*Pseudo*, ATCC 27853), and *Salmonella enterica* ssp. Arizonae (*Slmonella*, CIP 81-3), as well as *Staphylococcus aureus* (*S. Aureus*, ATCC 25923) as

Gram-positive bacterium. The fungi selected for antifungal assesses were *Aspergillus Niger* (*A. Niger, 939N*) and *Aspergillus Flavus* (*A. Flavus*, NRRL 3251). The microorganisms were kindly supplied by the applied microbiology laboratory (University of Bejaia, Algeria).

Antibacterial activity of clays was tested by agar diffusion method using Muller Hinton medium agar for bacteria and Potato Dextrose Agar PDA (semi-solid) for fungi. The test was initiated by pouring each agar onto sterilized Petri dishes and it was allowed to solidify. The surfaces of agar media were inoculated by overnight broth cultures of bacteria (10^8 CFU mL^{-1}) and fungi (10^6 spore mL^{-1}). Samples of sterile paper discs (9 mm) were steeped in clay overnight suspension (10 g mL^{-1}) and then deposited onto the inoculated agar and incubated at 37 °C for 24 h (bacteria) and at 28 °C for 5 days (fungi). The diameter of the clear zone around the sample was measured as an indication of inhibition of the microbial species. For comparison, similar disc diffusion tests were conducted using clay samples as dry pallets (50 mg). All tests were carried out in triplicate.

For the CA-based films, the antimicrobial efficiency was evaluated by both agar disc and vapour phase diffusion (disc volatilization) methods [25]. All samples were cut into 30 mm diameter discs, sterilized for 20 min by UV light. These media were inoculated as overhead procedure and the parafilm was used to tightly seal the Petri dishes to prevent any leakage of Th vapour. Films without active additives were used as control. Pure Th (3 mg) was also tested for comparison.

The disc volatilization method was applied to Th-included films. Briefly, the active films discs were adhered to the lid inside surface of the Petri plates, where no direct contact between the film sample and the bacterial or fungal agar media. The plates were sealed by parafilm, were turned upside down and then incubated as the above-mentioned protocol. During this time, the volatile Th released from samples was contacted with microorganisms on agar medium. In this test, the growth inhibition effects of active films were evaluated by agar plate counts of viable cells instead of clear inhibitory zones obtained in the direct contact diffusion test. After incubation, the bacteria colonies were counted and the inhibition reduction rate (%) was calculated according to Eq. (3).

$$\text{I} - \text{rate}\ (\%) = \frac{\text{CCD}_{\text{control}} - \text{CCD}_{\text{sample}}}{\text{CCD}_{\text{control}}} \times 100 \quad (3)$$

where I-rate (%) is the percent of inhibition rate; $CCD_{control}$ and CCD_{sample} are numbers of colonies counted in a culture disc of control bacteria and the antimicrobial film or Th samples, respectively.

3. Results and discussion

3.1. Evidence of silver nanoparticles formation inside the organoclay

The organoclay denoted OM was firstly prepared by inserting Ge chains, a typical amphoteric polyelectrolyte derivative of collagen with plenty of $–NH_2$ and –COOH groups, into MMt layers as previously reported [26]. The aim was to increase the d-spacing, favour the compatibility with CA matrix for subsequent formation of intercalated and/or exfoliation nanocomposite structures. Then, the biogenic synthesis of AgNPs was conducted *in situ* OM as solid carrier by using silver nitrate as precursor and *C. longa* tuber powder aqueous extract. The formation of AgNPs consisted of two steps (Fig. 1). Upon the addition of silver salt solution, the Ag^+ ions are absorbed and entrapped within OM. During the bio-reduction, the colour of the Ag^+-loaded OM suspension turned progressively from pale yellow that is originated from *C. longa* aqueous extract, to light brown, brown, and darker brown shades. This change in suspension colour highlights the formation of nano-sized silver particles embedded into OM originated from the surface plasmon resonance, resulting in a visible color change of clay from light gray to dark brown. Similar observations have be reported by Shameli et al. [13,14].

It is noteworthy that the boiling treatment during *C. longa* extraction would facilitate the release of some reductants that would play a key role in AgNPs formation in later stages.

Many researchers have focused on the mechanisms of biogenic synthesis of AgNPs and have explored the types of biomolecules present in plant extracts responsible for the reduction, formation

and stabilization of the nanoparticles. However, the exact mechanism is complex and still unexplored. Generally, it is established that the key factors for reducing of silver ions to nanoscale-sized particles are the polyphenols (terpenoids, flavonoids, tannins, polysaccharides) due to their electron donating ability, and in various extracts, they act as subsequent capping agent of AgNPs. While in others extracts, proteins may provide stabilizing effect since they are able to bind the nanoparticle surfaces and cap them, through either free amine and carboxylate groups or cysteine residues in the proteins [11-16].

The phytochemical analysis of C. longa rhizome extracts using different solvents (methanol, water, etc.) has evidenced the presence of such bioactive compounds like alkaloids, flavanoids, tannins, carbohydrates and proteins [36]. Curcumin is the most abundant phytochemical polyphenolic compound extracted from the powdered rhizomes of turmeric *of C. longa*. It has been reported to have a number of potentially beneficial biological activities, e.g., antioxidant, antimicrobial and anti-inflammatory properties. However, curcumin has an extremely poor water solubility (11.0 ng mL^{-1}) [37], and can be extracted by others solvents such as ethanol, methanol, acetone, and chloroform.

Therefore, the curcumin is not a key factor for the formation of the nano-sized silver particles owing to curcumin's water insolubility into the prepared aqueous *C. longa* tuber extract.

Based on the above-mentioned studies, analogous mechanism may operate in the present study. The water-soluble organic polyols compounds present in the aqueous *C. longa* tuber extract, such as flavones, terpenoids and polysaccharides, could present a dual functionality of reducing and capping Ag^{+} ions and subsequently stabilizing nascent AgNPs. Proteins molecules may probably act as potential capping agent and self-assemble on AgNPs surfaces via carboxylate groups. It should be mentioned that the analysis of nanoclays by FTIR spectroscopy, not presented in this paper, did not allow identifying the capping molecules because their functional groups bands are overlapped by those of the gelatin-MMt organoclay.

The presence of AgNPs within the organoclay was checked by UV/Vis diffuse reflectance spectroscopy. Fig. 2 depicts the absorption spectra of OM and its AgNPs-loaded OM in visible region together with that the *C. longa* extract. No band absorption was noticed for the OM and *C. longa*, while AgM displayed a broad band peaking at 409 nm emanating from the silver nanoparticles, indicating the occurrence of the quantum size surface plasmon resonance (SPR) [11-14]. Likewise, Sathishkumar et al. [15] monitored the biosynthesis of AgNPs using *C. longa* powder or aqueous extract periodically by UV/vis analysis and observed an increase in absorbance of the SPR band around 435 nm with respect to time reaction. Also, the appearance of this SPR band from 400 to 450 nm without further absorption evidenced the successful formation of well-segregated silver nano-sized particles [38].

Fig. 3a and b displays WAXS patterns of pristine Na^+M, OM, and AgM. From the low angles region (Fig. 3a), Na^+M exhibited a single diffraction peak at $2\theta = 6.62°$ ($d_{001} = 13.3$ Å), while this peak appeared in OM clay at lower angles $2\theta = 4.71°$ ($d_{001} = 18.7$ Å). This diffraction shifting highlights the intercalation of the Ge modifier into the clay. According to our previous studies [26,27], at pH < IEP, the Ge chains rich in NH_3^+ groups intercalate readily between the negatively charged MMt layers via electrostatic interactions. The surface modification of MMt outside interlayers is not to disregard.

From AgM WAXS pattern, the diffraction peak did not undergo appreciable shifting, indicating no further increase in d-spacing ($d_{001} = 18.6$ Å). Similarly, Sohrabnezhad et al. [39] prepared AgNPs-MMt using Urtica dioica leaf extract as reducing agent and they observed an irrelevant d-spacing increase from 12.4 Å in pure MMt to 12.9 Å in AgNPs-MMt. This result suggests that the formation of AgNPs did not occur wholly between the sillicates layers owing most likely to their larger sizes as compared to the available d-spacing. Indeed, the confined Ge chains might retard the penetration of Ag^+ ions into the inner space of the layers silicate, so that only a small amount of them can inserted

between sheets. As a result, the silver nucleation is delayed inside the clay galleries and occurred favourably close to the external layers surfaces.

From the wide angles region (Fig. 3b), The XRD patterns of all clay showed the presence of showed the presence of diffraction peaks of montmorillonite as main phase together with the presence of crystallites as impurities such as quartz (2θ = 19.8° and 26.6º) [40]. Compared to WAXS pattern of OM, the AgM exhibited extra diffraction peaks at 2θ = 37.84°, 46.72° that are indexed respectively to (111), (200) Bragg's reflections planes of face-centred cubic (FCC) crystalline structure of metallic silver (JCPDS 04-0783). Nevertheless, the expected diffraction peaks at around 64°, 76°, and 85° related to (220), (311), and (222) reflection planes of CFC phase are not perceptible due most likely to their overlapping by those of MMt or to their relative low intensities due to a low content of the embedded AgNPs within OM.

The formation of AgNPs was further confirmed by FESEM images. As observed in Fig.4, the white individual spots were ascribed to AgNPs, which are spherical in sharp with a smooth surface and mostly of uniform size with diameter ranging from ~ 7 nm to 40 nm. Additionally, some larger spots are obvious due to the presence of few aggregated nanoparticles.

The compositional determination of clays by EDX analysis is given in Fig. 4 (in Supplementary data). Unlike to the spectra of Na^+M and OM, the AgM spectrum showed a tiny peak at 3 keV which is in congruence with the major emission peaks specified for metallic silver due to surface plasmon resonance. The EDX results given in Table 2 highlighted the existence of a low amount of silver element. Also, the noteworthy reduction of sodium element in the OM indicated the successful Na^+ ions exchange process during the Ge-modification of MMt.

The quantification of the AgNPs into AgM was obtained from ICP-MS analysis, and the results are collected in Table 2. As expected, the highest composition of Ag element was detected in AgM

sample to be equal to 1.76 wt. %. This confirms once again the presence of silver nanoparticles inside AgM organoclay with a rather low content, in accordance with the above WAXS deductions.

The thermal degradation of clays was conducted under N_2 flow until 700 °C and continued under N_2/O_2 flow to 1000 °C to ascertain the presence of AgNPs into AgM. The TGA/d(TG) thermograms are shown in Fig.5 (in Supplementary data) and the obtained data are listed in Table 2.

Under inert atmosphere, all clays displayed an initial weight loss step below 200 °C due to moisture loss, which was more significant for Na^+MMt than both organoclays owing to its hydrophilic character. A second weight loss that appeared only for OM and AgM from 200 to 500 °C is attributed to the main decomposition of Ge chains. The last step starting at 520 °C and extended to 700 °C is due to the dehydroxylation of MMt layers [26,41,42]. It is noticed that the thermal decomposition rate of AgM is somewhat reduced compared to OM. This delay could be due to the high thermal resistance of the AgNPs [43]. The amount of AgNPs can be estimated from the difference in char values between AgM and OM at 700 °C, which is found to not exceed ~ 1.9 %.

After applying mixed N_2/O_2 atmosphere, both organoclays displayed an immediate oxidative decomposition from 700 to 800 °C, indicating a loss of residual inorganic compounds by the formation of metal oxides with the oxygen atoms scavenged from the TGA air atmosphere. In addition, the uppermost weight loss perceived for AgM provides once again an evidence for the existence of AgNPs.

TEM analysis was used as a most accurate technique to investigate the morphology, size and size distribution of the biosynthesized AgNPs within the OM. Fig.6a and b exhibits the TEM images and the resultant histogram of size nanoparticles distribution obtained. The AgNPs are spherical in shape at nanoscale levels and well segregated from one another across the MMt platelets. The obtained histogram showed a narrow size distribution of AgNPs in the size range of 2-35 nm with an average diameter about 6.92 ± 2.36 nm. This result suggests that the organoclay can also serve as an

appropriate carrier for the stabilization of the AgNPs, which are surrounded by the capping biomolecules extracted from *C. longa*. Indeed, some attractive interactions such as hydrogen bond may be developed between the functional groups of Ge chains (carboxylic, amine) and those of the capping molecules, offering an extra stabilizing effect, and so preventing AgNPs from further aggregation. In addition, the Ge protein chains may also interact with the AgNPs surface, through hydrogen bonding or electrostatic attractions, and thus providing further protection effect that is required for their stability [44].

3.2. CA-based nanocomposites study

3.2.1. Structural and morphological analysis

Fig. 7a and b displays the UV/Vis diffuse reflectance spectra of all CA-based films. In the range of 230–400 nm (Fig. 7a), all plasticized CA-based films showed a large absorption band centred at 278 nm, while no absorption was noticed for npC and TEC (as depicted in the inset). The appearance of this absorption in this region is due to a bathochromic shifting of the R band absorption of n $\rightarrow\pi^*$ transition related to the carbonyl of the acetate groups of CA, which is generally located at λ_{max} ~ 207 nm. This optical effect is caused by specific interactions, mainly hydrogen bonding developed between CA and TEC [45]. Indeed, the role of TEC polar groups is to reduce the inter-molecular H-bonds of CA chains to the benefit of their interactions with those of CA (acetate, hydroxyl) via hydrogen bonds and/or Van Der Waals dipolar forces.

Moreover, this band was more intense in the films including Th compared to their counterparts without Th additive. It is obvious that this R band overlapped the characteristic absorption band of thymol, which appeared in the same region at λ_{max} ~ 278 nm (as seen in the insert) [46,47].

Although the intensity of this band increases with the wt. % content of Th, it appeared less intense in pC films compared to nanocomposites. This result indicated that the retained Th amount is

slightly higher into ternary pC/AgM5/Th**z** nanocomposites than in pC/Th**z** films for the same initiating Th content. This behaviour could be ascribed to the clay delaying effect on the loss of Th by evaporation process during formulations preparation (drying, storage temperatures) through both tortuous path generation and chemical interactions (H-bonds), resulting in a fewer loss of Th amount in the final material. Similarly, Chen et al. [48] reported that the loss of mustard essential oil in the preparation of cellulose sulphate films was reduced by adding β-cyclodextrin. Tunç et al. [23] studied methyl cellulose/CRV/MMt nanocomposites and concluded that the inclusion of MMt causes a delay in the diffusion path of CRV molecules, which have to take a long way around the impermeable clay layers.

In the other hand, the plasmonic effect of AgNPs is highlighted in the visible range (400 –700 nm), Fig. 7b. The spectrum of pC did not show any absorption, while those of AgM-loaded films exhibited a single absorption at 439 nm, regardless of the Th content. This absorption is undoubtedly due to SPR of the biosynthesized nanoparticles. In addition, a red shift and broadness of this SPR band is perceived as compared to the spectrum of AgM. This result suggested the presence of AgNPs with higher size originated from the formation of some aggregates. It can be speculated that during the formulations processing the vigorous stirring promotes the release of few silver nanoparticles from the AgM into the matrix, causing the aggregation of some of them, and thus leading to an increase in the overall particles size distribution [49]. This speculation will be confirmed by TEM analysis.

Fig. 8a and b displays WAXS patterns of plasticized CA and its nano-hybrid films, prepared without and with Th. As it can be seen from the low angles region, all nanocomposites exhibited a diffraction peak that is shifted to lower angles, compared to each original clay diffraction, varying in a narrow range of 2θ = 1.92°– 1.98° (d_{001}= 46.0 – 44.6 Å). This highlights the intercalation of the plasticized CA chains within AgM clay. Similar intercalated structures were achieved by Rodríguez

et al. [28,29] and Park et al. [50] when CA was mixed with C30B using solution casting and melt processes, respectively. The driving forces for the formation of the intercalated structure could be due to polar interactions, mainly hydrogen bonding, between the polar groups (carbonyl, hydroxyl) of the confined CA/TEC chains and those of organophilic MMt [26,27,31]. The coexistence of exfoliated layers is however, not excluded. It should be mentioned that the organophilic treatment and the homogenization process (ultrasonic treatment) applied during the films preparation are promising factors for improving compatibility of the nanofiller with the CA matrix that promote the clay dispersion [51,52].

Compared to all other formulations, the binary pC/AgM3 nanocomposite displayed a lower intensity and broadening of this diffraction peak, suggesting the formation of a mainly exfoliated structure and/or relatively disordered structure with irregular interlayer distances. Beside, a basal diffraction was perceptible at $2\theta = 4.88°$ for the ternary pC/AgM5/Th8 formulation, indicating the coexistence of more aggregated platelets. In addition, this diffraction shifted slightly towards the wide angles as compared to the original AgM peak. This decrease in interlaminar distance is probably due to the release of few confined Ge chains between clay layers into the matrix during the formulations processing. Indeed, it is recognized from XRD patterns of polymer/natural or organophilic MMt nanocomposites that the shift of the peak position to lower angles (larger d-spacing) compared to that of original clay is generally taken as evidence of the matrix polymer intercalation into the clay galleries. However, an opposite shift may also occur for organically modified MMt, and this is usually attributed to loss of intercalant organic modifiers, such as surfactant from clay layers [53]. The possible coexistence of exfoliated structure will be further discussed in view of TEM images.

Further, useful structural information can be gathered by WAXS patterns in wide angles region, Fig. 8b. The pC pattern exhibited two prominent amorphous humps at around $2\theta \sim 9.2°$ and 18.8°, corresponding to d-spacing distances of ~ 10 and 4 Å, respectively. The first hump is originated from

short-range intermolecular order, i.e. the characteristic distance of two neighbouring cellulosic chains. It is the most affected by the TEC plasticizing effect. The second hump is due to the intramolecular order of two neighbouring anhydroglucose units [54]. Overall, both clay and Th additives caused an obvious decrease in the relative intensity of the first hump, indicating an alteration in the intermolecular distance between the CA and TEC. This result may be due to the occurrence of interactions, mostly hydrogen bonds, between the polar groups of pC and those of AgM as well as the hydroxyl groups of Th, which is expected to display the characteristic EOs plasticizing effect [26,27,32,55,56].

Further information on the morphology of the elaborated nano-biocomposites was provided by TEM analysis as a complementary technique. Fig. 9a-c shows TEM micrographs of typical pC/AgM**x** films and the resultant AgNPs size distribution histograms.

Overall, the TEM images showed that the morphology of nano-biocomposites is made up of mainly intercalated layered stacks of relatively small thickness together with some aggregated structures. Partially exfoliated silicate platelets randomly dispersed within CA matrix were also observed.

Besides, TEM images of both pC/AgM**x** nanocomposites revealed that AgNPs are spherical and are segregated uniformly from one another. However, it was noticed from Fig. 9b and c similar tendency to aggregate and a relatively larger size average and particles size distribution compared to the results obtained for AgM, i.e. 20.21 ± 5.26 nm for pC/AgM3 and 21.94 ± 6.50 nm for pC/AgM5. This result may originate from the formulations processing, in agreement with the forgoing UV/Vis deductions.

3.2.2. Thermal properties

The obtained DSC data of all films are listed in Table 3. As it can be seen, T_g and T_m values of virgin CA underwent a significant reduction upon plasticization by TEC by about 57 and 55 °C,

respectively. This decrease confirms the miscibility of TEC with the CA chains, and thus TEC is an efficient eco-friendly plasticizer that shifts the CA property from rigid to ductile since a significant reduction of its crystallinity degree is observed.

Overall, the addition of the AgM into the matrix at different loadings does not appreciably restrict the segmental motion of the CA chains, as evidenced by the slight shifting of Tg in all nanocomposites to higher values, by nearly a maximum of 8 °C, as compared to virgin pC film. A similar trend was observed for melting parameters (T_m, ΔH_m), while the crystallinity degree was somewhat enhanced. This result indicates that the added clay is not affecting significantly the amorphous phase of CA [57,58]. The explanation is confused since several combined factors may be involved such as the extent of the interactions nature at pC/clay platelets interface, and the clay dispersion degree [30,59].

The influence of the added thymol is more perceptible than the clay. Indeed, the incorporation of 4 and 8 wt. % of Th in the formulations reduced T_g of the CA matrix up to a maximum value of 14 °C. This behaviour is due to its plasticizing effect. The melting parameters (T_m, ΔH_m) and crystallinity grade were also depressed, indicating that Th hindered the CA crystallization. Similar results have been stated for CA and butyrate CAB or other polymer containing Th or other EOs [32,55,56,60,61].

The thermal stability of all CA-based films was assessed by TGA analysis, as displayed in Fig. 10 (in Supplementary data). The virgin CA displayed a single decomposition in the range of 255 - 420 °C due to the main chains degradation. The plasticized CA and its nanocomposites exhibited two additional steps due to weight losses of the associated TEC molecules with CA chains, which shifted to higher temperatures as compared to free TEC (as seen in the insert). The reported data in Table 3 included the temperature at 5 % of weight loss ($T_{5\%}$) which is considered as the onset degradation temperature (T_{onset}), maximum degradation temperature (T_{max}), and the residue at 575 °C. Compared to pC, the T_{max} values of all CA-based films ranged from 366 to 372 °C; however, T_{onset} shifted

slightly toward higher temperatures up to a maximum of 10 °C. Also, the addition of the clay increased the performance of the char formed at 575 °C, which acts as a superior insulator and efficient barrier to reduce the permeability to the volatile decomposition products [42,62]. The addition of thymol has not affected the CA matrix degradation profile since no obvious differences were noticed in both T_{onset} and T_{max} values for binary and ternary formulation films prepared with and without thymol. So, the thermal stability of the CA chains was rather improved by the clay nanofiller than other additives such as EOs.

3.2.3. Appearance and optical properties

UV barrier or transparency properties of the films having an average thickness of 73 ± 3 µm were evaluated from the transmittance (%) curves (Fig. 11) at 300 nm and 660 nm, and the results are shown in Table 4. The visual aspect of the freestanding flexible CA-based films, as observed in the insert, showed that pC film was highly transparent, while the nanocomposite films were translucent with the development of a brown colour owing to the nanoparticles plasmonic effect. The addition of Th did not influence the films appearance but they become more flexible than the free-Th films.

As expected, the neat pC film showed high T_{300} and T_{660} values in both UV and visible ranges of about 84 and 92 %, respectively. After the formation of nanocomposites, both values decreased with AgM loading; however, the decline level was more prominent for UV light. For instance, compared to pC film, the values of T_{300} and T_{660} of pC/AgM5 nanocomposite were declined by 39 % and 18 %, respectively. The reduced UV permeability can be owed to the mainly intercalated structure of the nanocomposites, which reflects and hinders the incoming light [26]. Moreover, the blocking of UV radiation passage is also triggered by the AgNPs, so that the scattered UV rays are lower in number [18, 44,63]. However, no obvious influence of the Th additive was noticed.

It should be mentioned that the UV resistance property is required in UV screening food packaging since it inhibits UV light driven reactions (lipid oxidation, discoloration, off-favours formation,...).

3.2.4. Mechanical properties

Nano-biocomposite films were analysed by means of tensile tests and the obtained results are collected in Table 4. As expected, the tensile modulus and elongation at break (%) were the most affected mechanical properties. Indeed, as the AgM content increased into pC matrix to 5 wt.%, the tensile modulus increased by 18% and the elongation decreased from 5 % to 2.5%, but a marginal effect on the tensile strength was noticed. Hence, the nano-biocomposite films become more brittle with the addition of the organoclay. A similar tensile tendency of CA/organoclay nanocomposites was obtained by Rodríguez et al. [28,29,32] and Lima et al. [30].

On the other hand, the incorporation of Th in the CA-based produced an antagonist effect. For instance, compared to pC film, the tensile modulus declined by about 9 % and 21 % for pC/Th4 and pC/Th8 films, respectively. In agreement with DSC analysis deductions, the addition of Th induced a plasticizing effect that altered the balance of interaction forces in the CA matrix, with a subsequent loss of film cohesion that facilitated chain mobility during film stretching, causing an increase in ductile properties. These common results, attesting that the addition of EOs to polymer films reduced the intermolecular chains interactions and produced materials with lower tensile strength, were broadly discussed in nanocomposites of cellulosic derivatives [32,55,56] and other polysaccharides [22,23,63].

It is also noted that the ternary systems pC/AgM5/Th**z** showed reduced values of elastic modulus as compared to pC film, suggesting that the Th plasticizing effect overcome over the reinforcement effect provided by the AgM. Similar Th effect was observed in poly(lactic acid) nanocomposites [64].

3.2.5. Oxygen barrier properties

The oxygen barrier properties of materials intended to be used in food packaging are of great importance since the presence of oxygen could decrease the food shelf-life. Thus, the CA-based films transmission rate per film thickness, expressed as normalized OTR (nOTR), are regrouped in Table 4. The nOTR values of all nanocomposite films containing were lower than that of the pC matrix, whatever the clay contents. The results indicate that the addition of clay enhanced the oxygen barrier properties due to the increment of diffusion path length. However, this retarding effect on traveling of oxygen molecules through matrix is not significant, which could be ascribed to the presence of predominantly intercalated layered silicate than exfoliated ones, in agreement with XRD and TEM findings. Indeed, an efficient dispersion of the clay platelets into the polymer matrix may form a tortuous pathway for gas molecules to permeate through the film. Comparable results were observed in nanocomposites of CAB/C30B [55,56] and CA/Cu^{2+}- MMt [65] with various clay loadings.

Besides, nOTR values increased by the added thymol, reflecting an improvement in oxygen permeability. This fact is associated with a Th plasticizing effect that facilitates the diffusional process of oxygen molecules through the matrix. In addition, the values of ternary pC/AgM5/Th**z** films were slightly lower than those of binary pC/Th**z** film counterparts, suggesting that the effect of clay on improving barrier properties overcomes the antagonist effect of thymol 64].

3.2.6. Antioxidant activity of films

Antioxidant food packaging is an efficient alternative to common ways such as the direct addition of antioxidants in food samples. In this way, the antioxidant activities of the binary pC/Th**z** and the ternary CA/AgM5/Th**z** formulation films were evaluated by the DPPH radicals scavenging ability.

The antioxidant capacity of each film extract was examined for 60 min into three food simulants: 10 % ethanol and 3% acetic acid as an aqueous and acidic food simulant, respectively, whereas 95 % ethanol was employed as fatty food simulant. From Table 5, the simulant 95 % ethanol promoted the release of greater amount of Th compound as evidenced by the highest values of DPPH inhibition. Although the mechanism is not wholly established, it is stated that the swelling of the polymer structure that occurred during the diffusion of simulant molecules into film could promote the migration of the active compound into the outer solution until thermodynamic equilibrium is attained [65-67]. Hence, the simulant 95 % ethanol give arise to more extent of plasticizing and/or swelling of the CA matrix, resulting in a faster diffusion of the Th molecules through a more flexible structure. The simulant 95 % ethanol was selected for the forthcoming experiments.

The kinetic of antioxidant activity of film extracts was also studied by measuring the scavenging activity against DPPH radicals, and the results are shown in Fig. 12 and Table 5. The DPPH inhibition values of all extracts sharply increased within early 60 min, and then begin to level off with the exposure time until 4 h, beyond which a steadying state was reached up to 90 % for a contact time of 9 h. Besides, a slight increase of the scavenging activity was noticed with an increase in Th content in each formulation. Also, the inhibition values of ternary systems were somewhat higher than of the binary counterpart films, regardless of the added Th concentration, as it is illustrated from Table 5. In accordance with the UV/Vis deductions, this result is most likely due to the delaying effect of the clay on the Th volatizing process during films drying and storage, resulting in an upper remaining Th amount in films. Another reason may be related to the tortuous path generation of the layered silicate, which could control the release of EOs from films [23]. Hence, the incorporating of into these nano-biocomposites supports their potential application as antioxidant food packaging.

3.2.7. Antimicrobial properties

The antimicrobial tests of both AgM and OM clays were carried out by agar diffusion disc against bacteria and fungi, which are commonly present in various kind of food products. Fig. 13 exhibits the typical antimicrobial results. After incubation, colonies of all tested bacteria and fungi were not viewed in the clear zone directly around AgM, while no inhibition zone was observed for OM control samples. These results indicated that the antimicrobial activity is ascribed solely to the AgPNs, regardless of their low amount (~1.7 wt.%), and the clay served only as carrier for stabilizing the nanoparticles [68]. The average values of the measured inhibition diameters (ID) are given in Table 6.

Although exact mechanisms of antimicrobial action of AgNPs are still in survey, it is recognized that Ag^+ ions are vital for antimicrobial activities and all the forms of silver are in one way or another sources of silver ions. Among them, the disruption of cell membrane via the interaction of AgNPs with sulphur-containing proteins and phosphorus-containing compounds like DNA, causing cell lyses. Another one, the disruption of peptidoglycan wall and cytoplasmatic membranes through electrostatic attractions between positive charged nanoparticles and negative charged bacteria cells [9-12].

An efficient antibacterial activity was obvious when the AgM samples were used as impregnated filter paper discs than as dry pellets. Indeed, when AgM is dispersed in a liquid medium, a greater release of silver ions occurred due to the oxidizing of nanoparticles by the dissolved oxygen ($O_{2\ (aq.)}$). In this case, the released silver ions are enough to generate superior antimicrobial activity against bacteria as reported by Sohrabnezhad et al. [39]. In addition, the inhibition action was higher against *E. Coli* than *S. Aureus* bacteria, showing ID values of 28 and 25 mm, respectively. Meanwhile, the *Salmonella* was the less sensitive bacterium. The less susceptibility of *S. Aureus* (Gram-positive bacterium) than *E. Coli* (Gram-negative bacterium) is due to its thicker cell wall that is makes up of more negatively charged peptidoglycan molecules, which

could trap more positively charged silver particles, so delaying their diffusion into *S. Aureus* cells [69].

Agar disc diffusion tests were also performed to examine the antimicrobial efficiency of CA-based films containing one or both active additives, as shown in Fig. 14a and Table 6. After incubation for 24 h, the binary pC/AgM**x** and the ternary pC/AgM5/Th**z** nano-biocomposites displayed low bacterial inhibition zone without any substantial differences. This moderate activity may be due mainly to the low AgNPs amount within the films, nearly 0.085 wt. % after adding 5 wt. % of AgM to matrix.

In the case of the binary pC/Th**z** films samples, no obvious inhibition halo appeared. This may be due to a sluggish diffusion of Th agent from sample, which may be not enough to reach a sufficient inhibition of bacterial growth in these conditions [61].

From the antifungal tests against *A. Niger* for 5 days, the active films showed moderate inhibition zones and lightening of floor covering through the petri plates, which indicated a decrease in fungi colonies density compared to control sample. This effect was more perceptible for Th-included films, suggesting an effectiveness action of thymol in these conditions. In addition, the ternary pC/AgM5/Th**z** nanocomposites exhibited effective antifungal activity as compared to pC/Th**z** counterpart films, where the highest growth inhibition was observed for sample prepared with 8 wt. % of Th. According to the forgoing deductions, it seems plausible to attribute this behaviour to the presence of a higher Th remaining content into the ternary formulated films, since the clay could control the release of thymol by retarding its vaporisation process. It is noteworthy that the antimicrobial activity of films is closely dependent on the direct contact of microbes with active agents. Thus, antimicrobial tests of films will be further explored under dynamic contact conditions using a quantitative shaking method [32,55].

Numerous studies [20-25, 67] stated that the volatilization (vapour phase) method is a systematic method for evaluating the antimicrobial effect of EOs compounds against pathogen

microorganisms. Hence, volatilization tests were conducted to ascertain the antimicrobial activity of the Th-included films, as illustrated in Fig. 14b and Table 6.

Overall, the T-included films exhibited an effectiveness of bacteria growth inhibition as compared to the direct contact by agar disc diffusion. As well, these films presented a remarkable antifungal activity against the tested *A. Niger* fungi with a similar trend effects as in agar test. Similarly, Pola et al. [27] reported that CA-based films incorporating oregano EO (20, 40 and 60 wt. %) and C30B (2.5 wt.%) presented more significant antifungal activity when applied in vapour phase.

As expected from Table 6, the most sensitive bacterium was *E. Coli*, while *Salmonella* bacterium showed the highest resistance. Also, the pC/AgM5/Th**z** nanocomposites displayed a slight decreased in inhibition rate as compared to the pC/Th**z** counterparts films. This effect is related to the added clay into the matrix that could retard the leakage of Th to the vapour phase, which is beneficial for a long-lasting antimicrobial effect. Previous studies ascribed the enhance in barrier transport of low molecular components such as EOs to the impermeable layered silicates [21-23]. Likewise, the synergistic interaction between MMt and thymol decreased the loss of EOs during processing, leading to actives nanocomposites with improved antimicrobial properties [70].

The antimicrobial action of EO compounds has been widely investigated against an extensive range of microorganisms, and several mechanisms have been proposed, among them, their ability in disrupting the fatty acid composition in cell wall, leading to cytoplasmic leakage and cell lysis.
These results allow us to make a preliminary inference that the CA nano-biocomposite films developed here could be promising antimicrobial packaging.

4. Conclusions

CA nano-biocomposite films based on renewable resources were developed by incorporating AgNPs/gelatin-MMt and thymol, with combined antimicrobial and antioxidant properties. The

results have evidenced the formation of mainly intercalated nano-biocomposites and have confirmed that both actives additives have influence on some properties. An increase in clay content declined the optical clarity but improved UV barrier properties. The addition of clay enhanced the tensile and oxygen barrier properties, while the thymol induced an antagonist effect. Also, The Tg value of matrix was decreased by the incorporated thymol, due to its plasticizing effect, whereas a slight enhance in thermal stability was provided by the clay nano-reinforcement. Significant antioxidant activities of thymol-including films were evidenced by the DPPH method. Finally, actives films showed combined antimicrobial activities against pathogenic bacteria and fungi, using disc diffusion method. *E. Coli* was found to be most sensitive to either AgNPs or thymol. However, the vapour phase method revealed an effective growth inhibition of thymol-included films. The presence of the organoclay may control silver release for a long-lasting antimicrobial effect.

These results point to the great potential of the ternary CA bio-nanocomposites as active packaging of different food products to extend their shelf life. This work will be extended to further investigations, mainly toxicological testing and migration studies of the active agents according to the standard conditions specified in the European food packaging regulations.

Acknowledgements

The authors are grateful to the laboratory of applied microbiology (faculty of natural and life sciences, University of Bejaia, Algeria, for providing necessary facilities.

References

[1] P. Cazón, G. Velazquez, J.A. Ramírez, M. Vàzquez, Polysaccharide-based films and coatings for food packaging: A review, Food Hydrocoll. 68 (2017) 136–148.

[2] I. Benito-González, A. López-Rubio, M. Martínez-Sanz, Potential of lignocellulosic fractions from Posidonia oceanica to improve barrier and mechanical properties of bio-based packaging materials, Int. J. Biol. Macromol. 118 Part A (2018) 542–551.

[3] R.A. Carvalho, T.A. Santos, V.M. Azevedo, P.H. C. Felix, M.V. Dias, S.V. Borges, Bio- nanocomposites for food packaging applications: effect of cellulose nanofibers on morphological, mechanical, optical and barrier properties, Polym. Int. 67 (2018) 386–392.

[4] N. Kumar, P. Kaur, S. Bhatia, Advances in bio-nanocomposite materials for food packaging: A review, Nutr. Food Sci. 47 (2017) 591–606.

[5] J.H.R. Llanos, C.C. Tadini, Preparation and characterization of bio-nanocomposite films based on cassava starch or chitosan, reinforced with montmorillonite or bamboo nanofibers, Int. J. Biol. Macromol. 107 Part A (2018) 371–382.

[6] S.M. Davachi, A.S. Shekarabi, Preparation and characterization of antibacterial, eco-friendly edible nanocomposite films containing Salvia macrosiphon and nanoclay, Int. J. Biol. Macromol. 113 (2018) 66–72.

[7] J. Wyrwa, A. Barska, Innovations in the food packaging market: active packaging, Eur. Food Res. Technol. 243 (2017) 1681–1692.

[8] J-W. Han, L. Ruiz-Garcia, J-P. Qian, X-T. Yang, Compr. Rev. Food Sci. Food Saf. 17 (2018) 860–877.

[9] V. Gomes, L. Souza, A.L. Fernando, Nanoparticles in food packaging: Biodegradability and potential migration to food: A review, Food Packag. Shelf Life 8 (2016) 63–70.

[10] K. Muthu, S. Priya, Green synthesis, characterization and catalytic activity of silver nanoparticles using *Cassia auriculata* flower extract separated fraction, Spectrochim. Acta A Mol. Biomol. Spectrosc. 179 (2017) 66–72.

[11] A. Chahardoli, N. Karimi, A. Fattahi, Nigella arvensis leaf extract mediated green synthesis of silver nanoparticles: Their characteristic properties and biological efficacy, Adv. Powder Technol. 29 (2018) 202–210.

[12] J.S. Moodley, S.B.N. Krishna, K. Pillay, S. Sershen, P. Govender, Green synthesis of silver nanoparticles from Moringa oleifera leaf extracts and its antimicrobial potential, Adv. Nat. Sci: Nanosci. Nanotechnol. 9 (2018) 15011-15020.

[13] K. Shameli, M.B Ahmad, A. Zamanian, P. Sangpour, P. Shabanzadeh, Y. Abdollahi, M. Zargar, Green biosynthesis of silver nanoparticles using *curcuma longa* tuber powder, Int. J. Nanomed. 7 (2012) 5603–5610.

[14] K. Shameli, M.B Ahmad, P. Shabanzadeh, E.A. Jaffar Al-Mulla, A. Zamanian, Y. Abdollahi, S.D. Jazayeri, M. Eili, F.A. Jalilian, R.Z. Haroun, Green biosynthesis of silver nanoparticles using *curcuma longa* tuber powder, Int. J. Nanomed. 7 (2012) 5603–5610.

[15] M. Sathishkumar, K. Sneha, Y.S. Yun, Immobilization of silver nanoparticles synthesized using *curcuma longa* tuber powder and extract on cotton cloth for bactericidal activity, Bioresource Technol. 101 (2010) 7958–7965.

[16] H. Ferfera-Harrar, D. Berdous, T. Benhalima, Hydrogel nanocomposites based on chitosan-g-polyacrylamide and silver nanoparticles synthesized using Curcuma longa for antibacterial applications, Polym. Bull. 75 (2018) 2819–2846.

[17] A. Roy, B.S. Butola, M. Joshi, Synthesis, characterization and antibacterial properties of novel nano-silver loaded acid activated montmorillonite, Appl. Clay Sci. 146 (2017) 278–285.

[18] J-W. Rhim, L-F. Wang, Preparation and characterization of carrageenan-based nanocomposite films reinforced with clay mineral and silver nanoparticles, Appl. Clay Sci. 97–98 (2014) 174–181.

[19] S. Girdthep, P. Worajittiphon, R. Molloy, S. Lumyong, T. Leejarkpai, W. Punyodom, Biodegradable nanocomposite blown films based on poly(lactic acid) containing silver-loaded kaolinite: A route to controlling moisture barrier property and silver ion release with a prediction of extended shelf life of dried longan, Polymer 55 (2014) 6776 – 6788.

[20] R. Ribeiro-Santos, M. Andrade, N. Ramos deMelo, A. Sanches-Silva, Use of essential oils in active food packaging: Recent advances and future trends, Trends Food Sci. Technol. 61 (2017) 132–140.

[21] M. Krepker, R. Shemesh, Y.D. Poleg, Y. Kashi, A. Vaxman, E. Segal, Active food packaging films with synergistic antimicrobial activity, Food Control 76 (2017) 117–126.

[22] K.A. Garrido–Miranda, B.L. Rivas, M.A. Pérez–Rivera, E.A. Sanfuentes, C. Peña-Farfal, Antioxidant and antifungal effects of eugenol incorporated in bionanocomposites of poly(3-hydroxybutyrate)-thermoplastic starch, LWT 98 (2018) 260–267.

[23] S. Tunç, O. Duman, Preparation of active antimicrobial methyl cellulose/carvacrol/ montmorillonite nanocomposite films and investigation of carvacrol release, LWT - Food Sci. Technol. 44 (2011) 465–472.

[24] D.M. Gouvêa, R.C.S. Mendonça, M.L. Soto, R.S. Cruz, Acetate cellulose film with bacteriophages for potential antimicrobial use in food packaging, LWT - Food Sci. Technol. 63 (2015) 85–91.

[25] G.S. Dannenberg, G.D. Funck, C.E.S. Cruxen, J.L. Marques, W.P. Silva, Â.M. Fiorentini, Essential oil from pink pepper as an antimicrobial component in cellulose acetate film: Potential for application as active packaging for sliced cheese, LWT - Food Sci. Technol. 81 (2017) 314–318.

[26] H. Ferfera-Harrar, N. Dairi, Elaboration of cellulose acetate nanobiocomposites using acidified gelatin-montmorillonite as nanofiller: morphology, properties, and biodegradation studies, Polym. Compos. 34 (2013) 1515–1524.

[27] H. Ferfera-Harrar, N. Dairi, Green nanocomposite films based on cellulose acetate and biopolymer‑modified nanoclays: studies on morphology and properties, Iran. Polym. J. 23 (2014) 917–931.

[28] F.J. Rodríguez, M.J. Galotto, A. Guarda, J.E. Bruna, Modification of cellulose acetate films using nanofillers based on organoclays, J. Food Eng. 110 (2011) 262–268.

[29] F.J. Rodríguez, A. Coloma, M.J. Galotto, A. Guarda, J.E. Bruna, Effect of organoclay content and molecular weight on cellulose acetate nanocomposites properties, Polym. Degrad. Stab.97 (2012) 1996–2001.

[30] J.A. Lima, C.A. Pinotti, M.I. Felisberti, M.C. Gonçalves, Morphology and mechanical properties of nanocomposites of cellulose acetate and organic montmorillonite prepared with different plasticizers, J. Appl. Polym. Sci. 124 (2012) 4628–4635.

[31] R.B. Romero, M.M.F. Ferrarezi, C.A.P. Leite, R.M.V. Alves, M.C. Goncalves, Influence of the layered silicate type on the structure, morphology and properties of cellulose acetate nanocomposite, Cellulose 20 (2013) 675–686.

[32] F.J. Rodríguez, H.M. Sepulveda, J.E. Bruna, A. Guarda, M.J. Galotto, Development of cellulose eco-nanocomposites with antimicrobial properties oriented for food packaging, Packag. Technol. Sci. 26 (2013) 149–160.

[33] C.C. Pola, E.A.A. Medeiros, O.L. Pereira, V.G.L. Souza, C.G. Otoni, G.P. Camilloto, N.F.F. Soares, Cellulose acetate active films incorporated with oregano (*Origanum vulgare*) essential oil and organophilic montmorillonite clay control the growth of phytopathogenic fungi, Food Packag. Shelf Life 9 (2016) 69–78.

[34] D.A. Cerqueira, G. Rodrigues, R.M.N. Assuncao, A new value for the heat of fusion of a perfect crystal of cellulose acetate, Polym. Bull. 56 (2006) 475–484.

[35] Y. Byun, Y.T. Kim, S. Whiteside, Characterization of an antioxidant polylactic acid (PLA) film prepared with α-tocopherol, BHT and polyethylene glycol using film cast extruder. J. Food Eng. 100 (2010) 239–244.

[36] A. Guptaa, S. Mahajana, R. Sharma, Evaluation of antimicrobial activity of *curcuma longa* rhizome extract against Staphylococcus aureus, Biotechnol. Reports 6 (2015) 51–55.

[37] K. Ahmed, Y. Li, D.J. Clements, H. Xiao, Nanoemulsion- and emulsion-based delivery systems for curcumin: Encapsulation and release properties, Food Chem. 132 (2012) 799–807.

[38] A. Chhatre, P. Solasa, S. Sakle, R. Thaokar, A. Mehra, Color and surface plasmon effects in nanoparticles systems: case of silver nanoparticles prepared by micro-emulsion route. Colloids Surf. A Physicochem. Eng. Aspects 404 (2012) 83–92.

[39] S. Sohrabnezhad, M. Rassa, A. Saifi, Green synthesis of Ag nanoparticles in montmorillonite, Mater. Lett. 168 (2016) 28–30.

[40] C.I.R. Oliveira, M.C.G. Rocha, A.L.N. da Silva, L.C. Bertolino, Characterization of bentonite clays from Cubati, Paraíba (Northeast of Brazil) Cerâmica 62 (2016) 272–277.

[41] J.F. Martucci, A. Vázquez and R.A. Ruseckaite, Nanocomposites based on gelatin and montmorillonite morphological and thermal studies, J. Therm. Anal. Calorim. 89 (2007) 117–122.

[42] A. Choudhury, A.K. Bhowmick, C. Ong, M. Soddemann, Effect of various nanofillers on thermal stability and degradation kinetics of polymer nanocomposites, J. Nanosci. Nanotechnol. 10 (2010) 5056–5071.

[43] J.W. Rhim, L.F. Wang, S.I. Hong, Preparation and characterization of agar/silver nanoparticles composite films with antimicrobial activity, Food Hydrocoll. 33 (2013) 327–335.

[44] C. Dong, X. Zhang, H. Cai, Green synthesis of monodisperse silver nanoparticles using hydroxyl propyl methylcellulose, J. Alloys Compd. 583 (2014) 267–271.

[45] T. Ganguly, S.B. Banerjee, Effect of hydrogen bonding on the electronic absorption spectra of xylenols, Spectrochim. Acta A Mol. Spectrosc. 34 (1978) 617–623.

[46] H. Hajimehdipoor, M. Shekarchi, M. Khanavi, N. Adib, M. Amri, A validated high performance liquid chromatography method for the analysis of thymol and carvacrol in Thymus vulgaris L. volatile oil, Phcog. Mag. 6 (2010) 154–158.

[47] A. Rukmani, M. Sundrarajan, Inclusion of antibacterial agent thymol on β-cyclodextrin-grafted organic cotton, J. Ind. Text. 42 (2015) 132–144.

[48] G. Chen, B. Liu, Cellulose sulfate based film with slow-release antimicrobial properties prepared by incorporation of mustard essential oil and β–cyclodextrin, Food Hydrocoll. 55 (2016) 100–107.

[49] D. Maity, M.R. Mollick, D. Mondal, B. Bhowmick, M.K. Bain, K. Bankura, J. Sarkar, K. Acharya, D. Chattopadhyay, Synthesis of methylcellulose silver nanocomposite and investigation of mechanical and antimicrobial properties, Carbohyd. Polym. 90 (2012) 1818–1825.

[50] H-M. Park, M. Misra, L.T. Drzal, A.K. Mohanty, "Green" nanocomposites from cellulose acetate bioplastic and clay: effect of eco-friendly triethyl citrate plasticizer, Biomacromolecules 5 (2004) 2281–2288.

[51] K. Majdzadeh-Ardakani, A.H. Navarchian, F. Sadeghi, Optimization of mechanical properties of thermoplastic starch/clay nanocomposites, Carbohyd. Polym. 79 (2010) 547–554.

[52] K. Müller, E. Bugnicourt, M. Latorre, M. Jorda, Y.E. Sanz, J.M. Lagaron, O. Miesbauer, A. Bianchin, S. Hankin, U. Bölz, G. Pérez, M. Jesdinszki, M. Lindner, . Scheuerer, S. Castelló, M. Schmid, Review on the processing and properties of polymer nanocomposites and nanocoatings and their applications in the packaging, automotive and solar energy fields, Nanomaterials, 74(2017) 1–47.

[53] D.R. Paul, L.M. Robeson, Polymer nanotechnology: Nanocomposites, Polymer 49 (2008) 3187–3204.

[54] T.G. Fawcett, C.E. Crowder, S.N. Kabekkodu, F. Needham, J.A. Kaduk, T.N. Blanton, V. Petkov, E. Bucher, R. Shpanchenko, Reference materials for the study of polymorphism and crystallinity in cellulosics. Powder Diffraction, 28 (2013) 18–31.

[55] R.I. Quintero, F. Rodriguez, J. Bruna, A. Guarda, M.J. Galotto, Cellulose acetate butyrate nanocomposites with antimicrobial properties for food packaging, Packag. Technol. Sci. 26 (2013) 249–265.

[56] R.I. Quintero, M.J. Galotto, F. Rodriguez, A. Guarda, Preparation and characterization of cellulose acetate butyrate/organoclay nanocomposites produced by extrusion, Packag. Technol. Sci. 27 (2014) 495–507.

[57] Y.A. Arfat, M. Ejaz, H. Jacob, J. Ahmed, Deciphering the potential of guar gum/Ag-Cu nanocomposite films as an active food Packaging material, Carbohyd. Polym. 157 (2017) 65–71.

[58] P.F. Andrade, A. Fonseca de Faria, F.J. Quites, S.R. Oliveira, O.L. Alves, M.A.Z. Arruda, M.C. Gonçalves, Inhibition of bacterial adhesion on cellulose acetate membranes containing silver nanoparticles, Cellulose 22 (2015) 3895–3906.

[59] J.H.R. Llanos, C.C. Tadini, Preparation and characterization of bio-nanocomposite films based on cassava starch or chitosan, reinforced with montmorillonite or bamboo nanofibers, Int. J. Biol. Macromol. 107 Part A (2018) 371–382.

[60] M. Ramos, E. Fortunati, M. Peltzer, F. Dominici, A. Jiménez, M.C. Garrigós, J.M. Kenny, Influence of thymol and silver nanoparticles on the degradation of poly(lactic acid) based nanocomposites: Thermal and morphological properties, Polym. Degrad. Stab. 108 (2014) 158-165.

[61] M. Ramos, A. Jiménez, M. Peltzer, M.C. Garrigós, Characterization and antimicrobial activity studies of polypropylene films with carvacrol and thymol for active packaging, J. Food Eng. 109 (2012) 513–519.

[62] Y. Cui, S. Kumar, B. Rao Kona, D. van Houcke, Gas barrier properties of polymer/clay nanocomposites, RSC Adv. 5 (2015) 63669–63690.

[63] P. Kanmani, J.M. Rhim, Physical, mechanical and antimicrobial properties of gelatin based active nanocomposite films containing AgNPs and nanoclay, Food Hydrocoll. 35 (2014) 644–652.

[64] J.E. Bruna, M.J. Galotto, A. Guarda, F. Rodríguez, A novel polymer based on $MtCu^{2+}$ /cellulose acetate with antimicrobial activity, Carbohyd. Polym. 102 (2014) 317–323.

[65] M. Ramos, A. Jiménez, M. Peltzer, M.C. Garrigós, Development of novel nano-biocomposite antioxidant films based on poly (lactic acid) and thymol for active packaging, Food Chem. 162 (2014) 149–155.

[66] V. Muriel-Galet, M.J. Cran, S.W. Bigger, P. Hernández-Muñoz, R. Gavara, Antioxidant and antimicrobial properties of ethylene vinyl alcohol copolymer films based on the release of oregano essential oil and green tea extract components, J. Food Eng. 149 (2015) 9–16.

[67] J.R. Calo, P.G. Crandall, C.A. O'Bryan, S.C. Ricke, Essential oils as antimicrobials in food systems A review, Food Control 54 (2015) 111–119.

[68] F. Xu, B. Weng, L.A. Materon, A. Kuang, J.A. Trujillo, K. Lozano, Fabrication of cellulose fine fiber based membranes embedded with silver nanoparticles via Force spinning, J. Polym. Eng. 36 (2015) 269–278.

[69] F. Xu, B. Weng, R. Gilkerson, L.A. Materon, K. Lozano, Development of tannic acid/chitosan/pullulan composite nanofibers from aqueous solution for potential applications as wound dressing, Carbohydr. Polym. 115 (2015) 16–24.

[70] R. Efrati, M. Natan, A. Pelah, A. Haberer, E. Banin, A. Dotan, A. Ophir, The combined effect of additives and processing on the thermal stability and controlled release of essential oils in antimicrobial films, J. Appl. Polym. Sci. 131(2014) 40564–40571.

Figures captions

Fig. 1. Biogenic synthesis of AgNPs *in situ* gelatin-MMt organoclay using *C. longa* tuber powder aqueous extract.

Fig. 2. UV/Vis reflected diffusion spectra of OM and AgNPs-loaded OM clays together with that the *C. longa* extract.

Fig. 3. WAXS patterns of nanoclays observed in (a) low angles and (b) wide angles regions (M: Montmorillonite, Q: Quartz, Ag°: AgNPs).

Fig. 4. FESEM images of organoclays together with the EDX spectra.

Fig. 5. TGA and d(TG) thermograms of pristine MMt and organically modified OM and AgM.

Fig. 6. (a) TEM images of AgM organoclay and (b) the corresponding AgNPs size nanoparticles distribution histogram.

Fig. 7. UV/Visible diffuse reflectance spectra of CA-based films (a) in UV light region (the insert shows the spectra of TEC and Th); (b) in visible region.

Fig. 8. WAXS patterns of plasticized CA and its nano-biocomposites observed in (a) low angles region ($2\theta = 1.5 – 8°$) together with AgM, and (b) in wide angles region ($2\theta = 5 – 60°$).

Fig. 9. (a) TEM micrographs of CA nano-biocomposites denoted (4) pC/AgM3 and (5) pC/AgM5), using high magnifications (100, 50, 20 and 10 nm scale bar); AgNPs size distribution histograms (c) and (d) of pC/AgM3 and pC/AgM5 films, respectively.

Fig.10. TGA and d(TG) thermograms of plasticized CA-based films (the insert shows the curves of virgin CA, TEC, and their physical mixture).

Fig. 11. Transmittance (%) versus wavelength curves of CA-based films (the insert shows visual optical clarity). (0) npC, (1) pC, (2) pC/Th4, (3) pC/Th8, (4) pC/AgM3, (5) pC/AgM5, (6) pC/AgM5/Th4, (7) pC/AgM5/Th8.

Fig. 12. Kinetic of DPPH radical scavenging ability of CA-based films including Th (the insert shows Th-included film extracts obtained at different exposure times. (Th) Thymol, (As.A) Ascorbic acid, (1) pC, (2) pC/Th4, (3) pC/Th8, (6) pC/AgM5/Th4, (7) pC/AgM5/Th8.

Fig. 13. Disc diffusion tests of the antimicrobial activity of OM and AgM organoclays against bacteria and fungi. The tested samples are (a) filter paper impregnated with clay suspension and (b) clay pellets.

Fig. 14. Antimicrobial activities outcomes of CA-based films and thymol alone against pathogenic bacteria and fungi using (a) agar disc diffusion tests and (b) volatilization method (only for active T-included films). (1) pC, (2) pC/Th4, (3) pC/Th8, (4) pC/AgM3, (5) pC/AgM5, (6) pC/AgM5/Th4, (7) pC/AgM5/Th8, (control) microorganism, (Th) Thymol.

Table 1

Cellulose acetate based films formulated at different contents of additives

Sample	Code	CA	TEC	AgM organoclay		Thymol	
		m (g)	m (g)	m (g)	**x** (wt.%)[a]	m (g)	**z** (wt.%)[a]
pC	(1)	1	0.2	0	0	0	0
pC/Th**z**	(2)	1	0.2	0	0	0.04	4
	(3)	1	0.2	0	0	0.08	8
pC/AgM**x**	(4)	1	0.2	0.03	3	0	0
	(5)	1	0.2	0.05	5	0	0
pC/AgM**x**/Th**z**	(6)	1	0.2	0.05	5	0.04	4
	(7)	1	0.2	0.05	5	0.08	8

[a] Weight ratio (%) with respect to CA matrix.

Table 2

Elemental composition and TGA parameters of pristine and modified MMt clays.

Clay sample	Elemental analysis (wt. %)				TGA analysis						
	ICP-MS		EDX		Step 2[a]		Step 3[b] (until 700 °C)			Step 4[c]	
	Na	Ag	Na	Ag	T_{max} (°C)	Wt. loss (%)	T_{max} (°C)	Wt. loss (%)	Char (%)	T_{max} (°C)	Wt. loss (%)
$Na^{+}M$	1.205	…….	1.31±0.52	…….	…….	…….	630	2.636	86.47	…….	…….
OM	0.143	…….	0.41±0.07	…….	352	19.28	574	2.610	72.93	716.5	6.133
AgM	0.046	1.765	……..	1.61±0.44	354	18.15	575	2.634	74.84	717.5	7.863

[(a,b), c] Thermal degradation under N_2 atmosphere (30 - 700 °C) and N_2/O_2 atmosphere (700-1000 °C), respectively.

Table 3

TGA and DSC parameters obtained for CA and all CA-based nano-biocomposite films.

Sample (Code)		TGA analysis						DSC analysis			
		$T_{1\,max}$ – Wt. $loss_1$		$T_{2\,max}$ –Wt. $loss_2$		$T_{3\,(5\%)}$	$T_{3\,max}$	Wt. $loss_3$	Char at 575 °C	T_g	T_m	ΔH_m	χ
		(°C)	(%)	(°C)	(%)	(°C)[a]	(°C)	(%)	(%)	(°C)[c]	(°C)[b]	(J/g)[c]	(%)[c]
pC	(1)	215	4.75	287	17.28	335	366	63.36	11.95	126	164	0.275	0.561
pC/Th4	(2)	212	8.35	292	14.05	337	367	63.34	11.64	121	161	0.023	0.049
pC/Th8	(3)	207	8.06	283	15.17	336	367	62.65	11.09	115	n.d	n.d	n.d
pC/AgM3	(4)	220	5.98	295	15.51	338	365	61.36	14.22	129	167	0.218	0.456
pC/AgM5	(5)	220	6.80	303	9.72	341	371	67.48	13.00	131	168	0.235	0.500
pC/AgM5/Th4	(6)	218	7.66	299	11.78	345	370	66.19	12.13	127	165	0.079	0.173
pC/AgM5/Th8	(7)	212	10.4	298	10.56	344	370	64.14	12.02	117	n.d	n.d	n.d

[a] T_{onset} of the third thermal decomposition; [b]Determined from the second scan; [c] Based on $\Delta H°_m$ (100 % crystalline sample) = 58.8 J g^{-1}; n.d: not detected.

Table 4

Mechanical properties, oxygen transmission rate and optical properties obtained for all the studied formulations.

Sample[a]	Tensile parameters [b]			Barrier properties to oxygen [c]	Optical properties [d]	
	Elastic Modulus, *E* (MPa)	Strength, TS (MPa)	Elongation at break, EB (%)	nOTR (cm^3 mm m^{-2} day^{-1})	$\%T_{300\ nm}$	$\%T_{660\ nm}$
pC	2061 ± 112	45.51 ± 0.92	5.10 ± 1.66	55.67 ± 2.56	82.6	92.0
pC/Th4	1870 ± 130	42.44 ± 1.22	6.17 ± 0.72	59.84 ± 3.62	80.0	91.5
pC/Th8	1625 ± 144	36.64 ± 1.94	7.77 ± 1.86	66.82 ± 2.54	79.0	91.6
pC/AgM3	2211 ± 125	46.85 ± 1.32	3.39 ± 0.44	51.30 ± 2.24	54.6	78.8
pC/AgM5	2436 ± 74	48.28 ± 2.42	2.55 ± 0.24	48.10 ± 3.67	43.3	73.7
pC/AgM5/Th4	2084 ± 117	45.24 ± 1.36	3.04 ± 0.19	57.35 ± 3.32	37.4	71.1
pC/AgM5/Th8	1882 ± 106	42.92 ± 1.42	3.72 ± 0.01	63.26 ± 4.37	38.2	70.0

[a] pC film was used as control; [b] n = 5, mean ± SD; [c] n = 3, mean ± SD; [d] Transmittance (%) of light in UV and visible regions.

Table 5

Radical scavenging activity of DPPH radical into different simulants for CA-based films containing thymol.

Sample	Extract/DPPH: 2/1 (v/v) into simulants [a]			Extract/DPPH: 1/1 (v/v) [b]	
	3% acetic acid	10 % ethanol	95 % ethanol	1 h	9 h
pC/Th4	81.93	76.53	90.54	77.50	86.38
pC/Th8	84.52	79.00	91.06	78.62	87.66
pC/AgM5/Th4	83.16	79.44	93.45	81.76	89.05
pC/AgM5/Th8	85.12	81.07	94.04	83.03	90.55

[a] DPPH inhibition values for 1h; [b] Exposure times of film extracts from kinetic study in 95 % ethanol.

Table 6

Antimicrobial effect of nanosilver particles-included organoclay and/or thymol in the CA-based nano-biocomposite films.

Sample	Disc diffusion method tests against bacteria and fungi [a,b]											
	E. Coli		*S. Aureus*		*Salmonella*		*Pseudomonas*		Aspergillus *Niger*		Aspergillus *Flavus*	
	I.D (mm)		I.D (mm)		I.D (mm)		I.D (mm)		I.D (mm)		I.D (mm)	
OM	9	9	9	9	9	9	9		9		9	
AgM	28 ± 0.8[a]	15 ± 0.6[b]	25 ± 0.5[a]	12 ± 0.2[b]	20 ± 0.2[a]	10 ± 0.3[b]	25.5 ±1		22.5 ±0.6		19 ±0.2	
	Disc diffusion method against bacteria [c]						Vapour phase method against bacteria [d]					
	E. Coli		*S. Aureus*		*Salmonella*		*E. Coli*		*S. Aureus*		*Salmonella*	
	I.D (mm)		I.D (mm)		I.D (mm)		CCD	I-rate (%)	CCD	I-rate (%)	CCD	I-rate (%)
Control strain	….		….		….		283	….	290	….	289	….
Thymol	9		9		9		24 ± 2	91.81	46 ± 3	84.14	102 ± 2	64.70
pC/Th4	30		30		30		96 ± 5	67.23	130 ± 1	55.17	179 ± 0	38.06
pC/Th8	30		30		30		72 ± 3	75.43	100 ± 2	65.51	157 ± 3	45.67
pC/AgM3	33		32		31		….	….	….	….	….	….
pC/AgM5	36		34		31		….	….	….	….	….	….
pC/AgM5/Th4	35		33		32		131 ± 0	55.30	147 ± 2	49.31	195 ± 3	32.52
pC/AgM5/Th8	35		34		32		103 ± 2	64.84	121 ± 4	58.27	159 ± 1	45.06

[a,b, c] Disc diffusion method using samples of impregnated filter paper, pallets, and films, respectively. Diameter (average value) of inhibition zone (mm) including the diameter of the samples disc: 9 mm for clays and Th; 30 mm for films. [d] CCD: colony in a culture plate; I-rate: inhibition rate.

Highlights

- Biogenic synthesis of silver nanoparticles (AgNPs) inside gelatin-montmorillonite (AgM) using *Curcuma longa* tuber aqueous extract as both reducing and capping agent.

- Preparation of binary and ternary cellulose acetate (CA)-based nano-biocomposite films using AgM clay and/or thymol as active additives.

- Improvement in tensile properties, UV blocking, and oxygen barrier capability of the films containing AgM.

- Efficient antioxidant activity of films containing thymol.

- Synergistic effects of AgNPs and thymol on the antimicrobial and antifungal activities of the bionanocomposites films.

- Potential application of ternary bionanocomposite films as active food packaging.

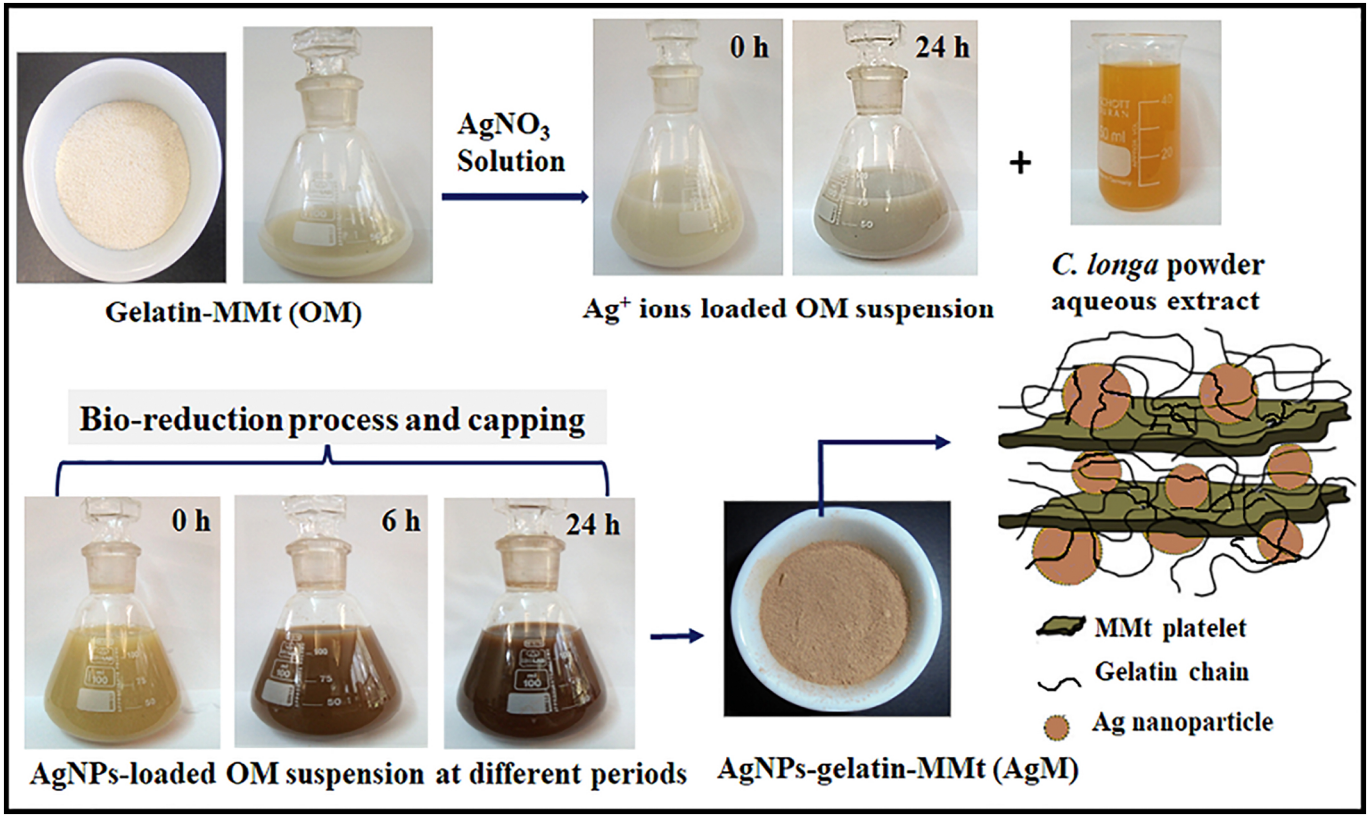
Gelatin-MMt (OM)
AgNO3 Solution
0 h
24 h
Ag+ ions loaded OM suspension
+
C. longa powder aqueous extract
Bio-reduction process and capping
0 h
6 h
24 h
AgNPs-loaded OM suspension at different periods
AgNPs-gelatin-MMt (AgM)
MMt platelet
Gelatin chain
Ag nanoparticle

Figure 1

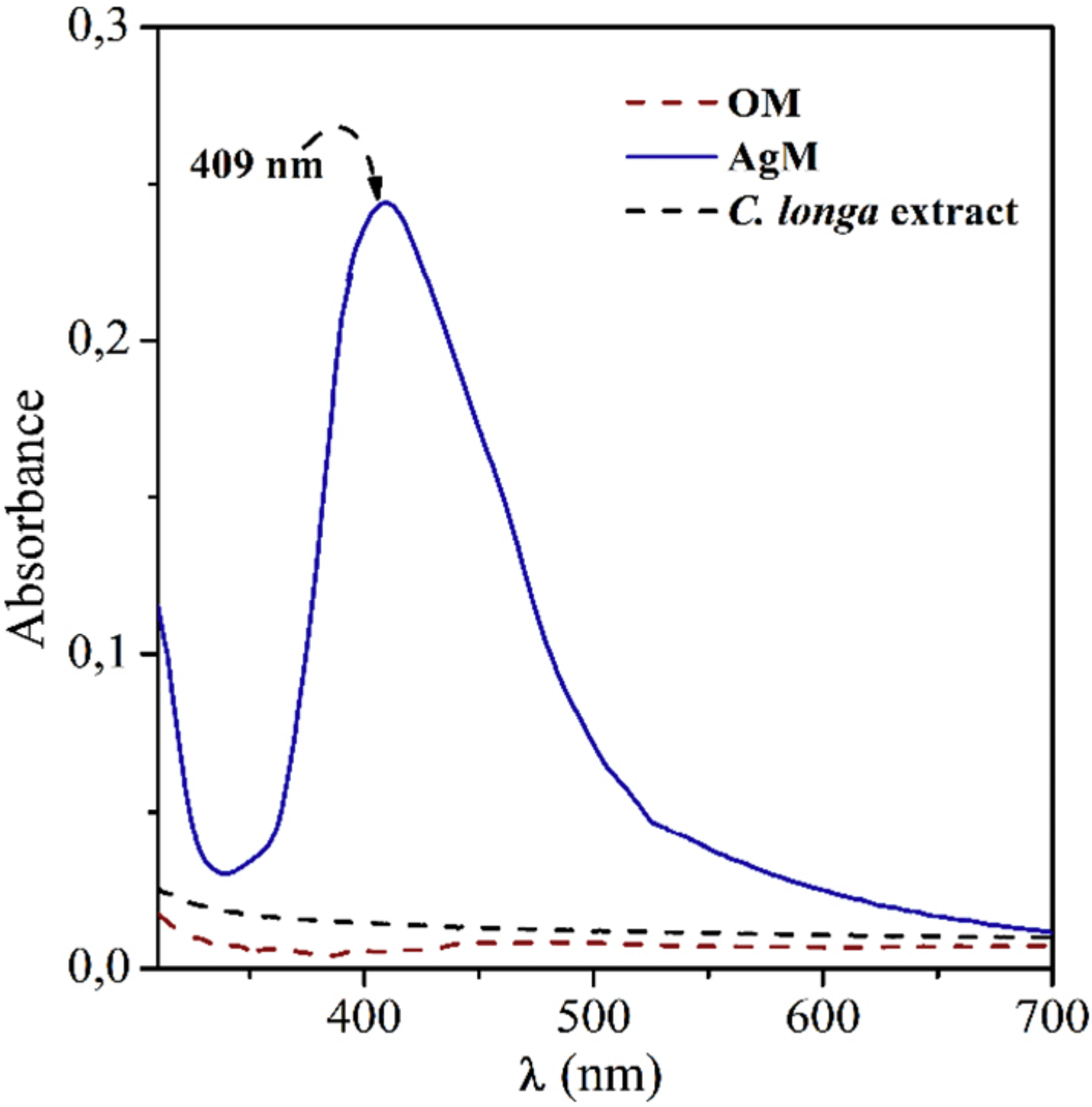
0,3
0,2
0,1
0,0
Absorbance
409 nm
OM
AgM
C. longa extract
400
500
600
700
λ (nm)

Figure 2

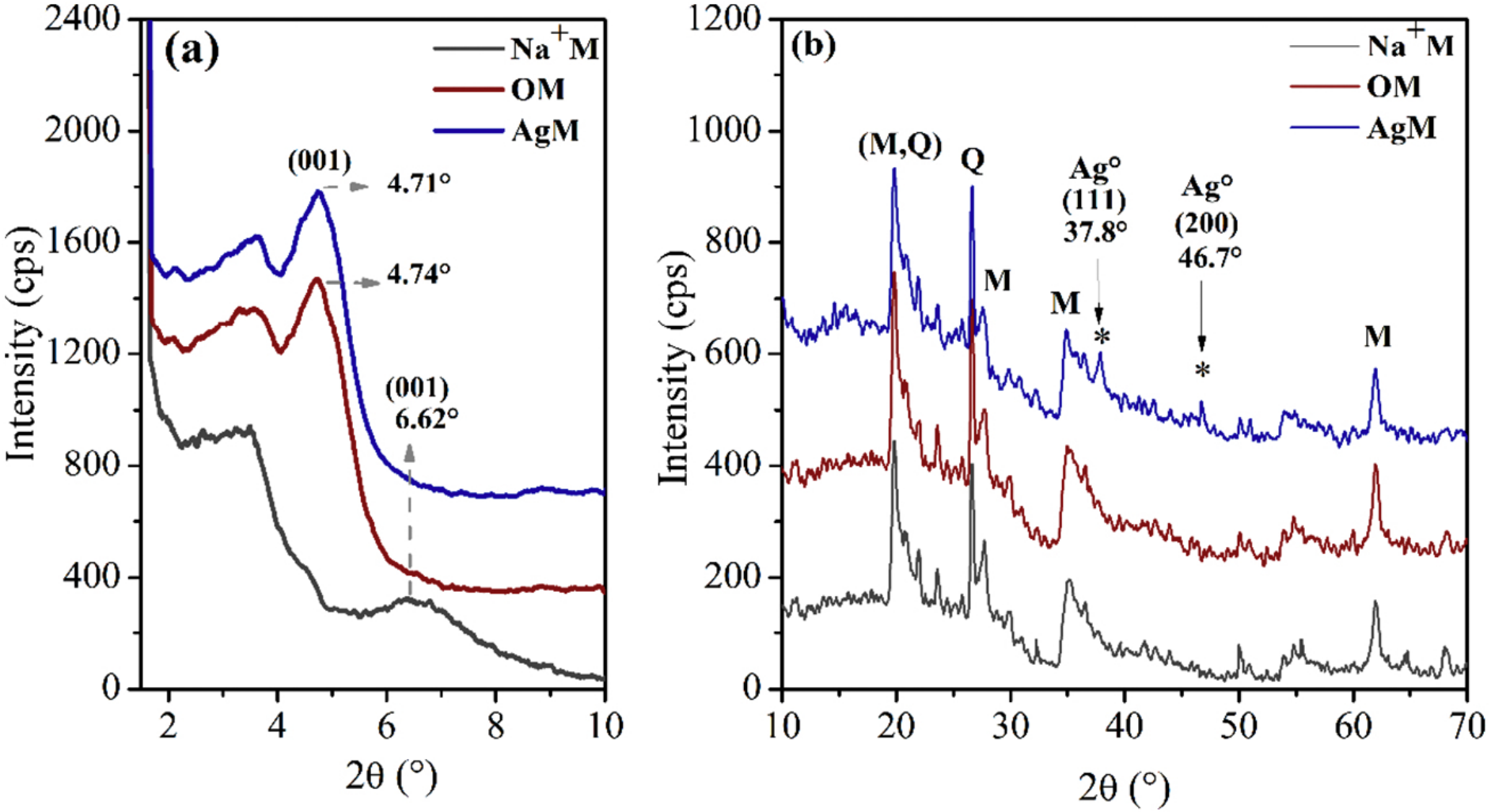
(a)
Na+M
OM
AgM
(001)
4.71°
4.74°
(001)
6.62°
Intensity (cps)
2θ (°)
(b)
Na+M
OM
AgM
(M,Q)
Q
M
M
Ag°
(111)
37.8°
Ag°
(200)
46.7°
*
*
M
Intensity (cps)
2θ (°)

Figure 3

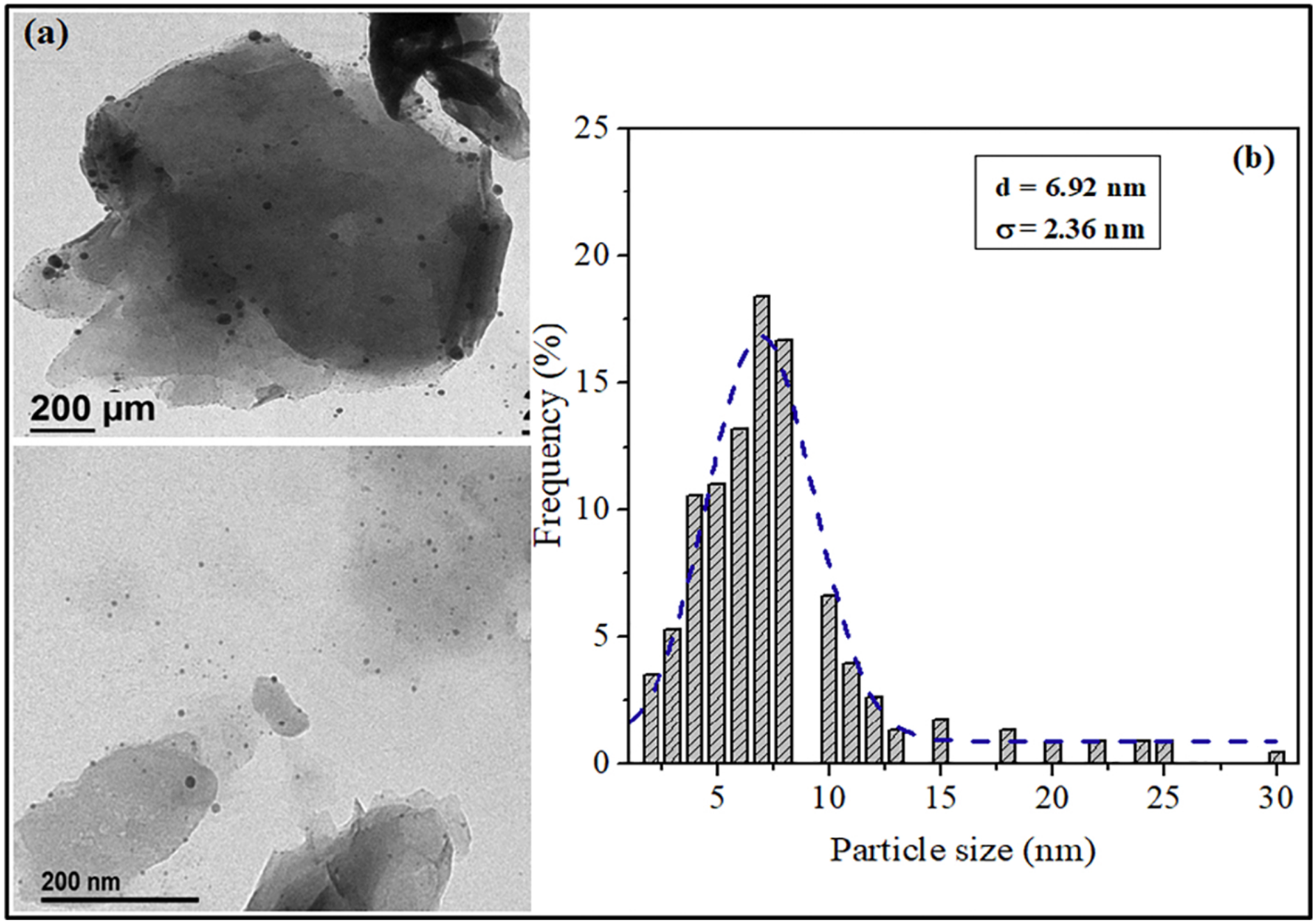
(a)
200 µm
200 nm
(b)
d = 6.92 nm
σ = 2.36 nm
Frequency (%)
Particle size (nm)
0
5
10
15
20
25
30

Figure 4

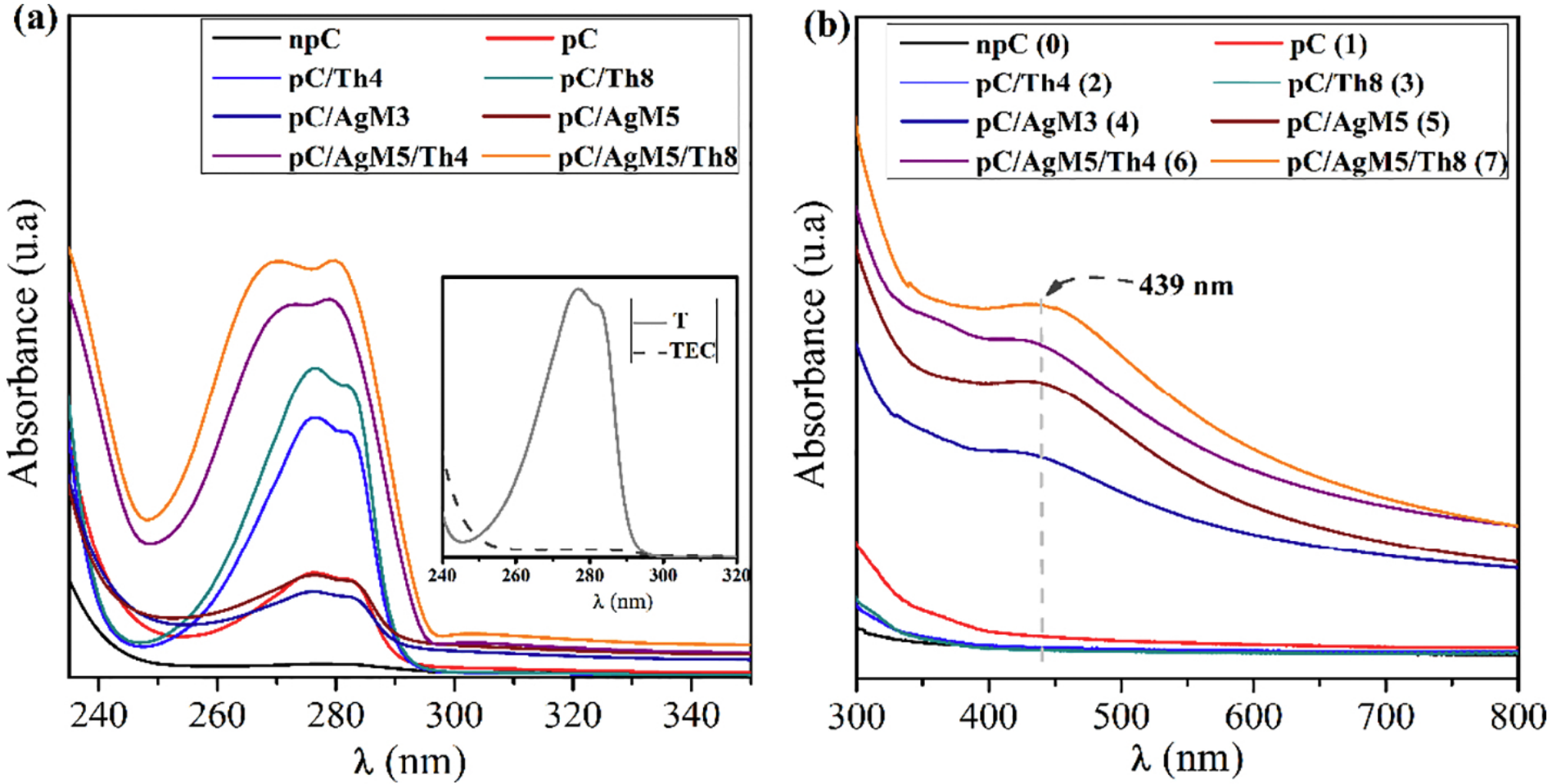
(a)
npC
pC
pC/Th4
pC/Th8
pC/AgM3
pC/AgM5
pC/AgM5/Th4
pC/AgM5/Th8
Absorbance (u.a)
λ (nm)
T
-TEC
(b)
npC (0)
pC (1)
pC/Th4 (2)
pC/Th8 (3)
pC/AgM3 (4)
pC/AgM5 (5)
pC/AgM5/Th4 (6)
pC/AgM5/Th8 (7)
439 nm

Figure 5

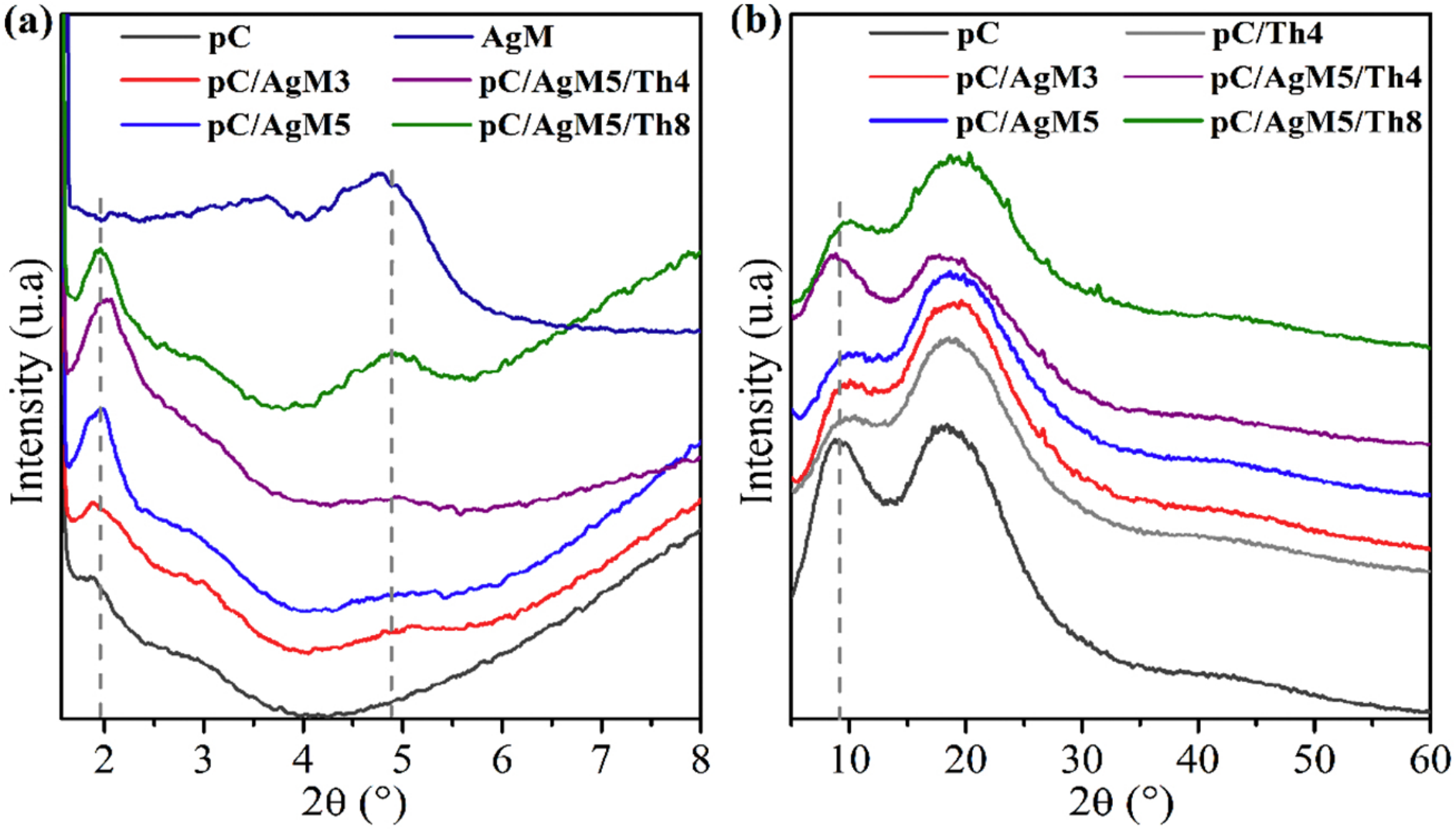
(a)
pC
AgM
pC/AgM3
pC/AgM5/Th4
pC/AgM5
pC/AgM5/Th8
Intensity (u.a)
2θ (°)
(b)
pC
pC/Th4
pC/AgM3
pC/AgM5/Th4
pC/AgM5
pC/AgM5/Th8
Intensity (u.a)
2θ (°)

Figure 6

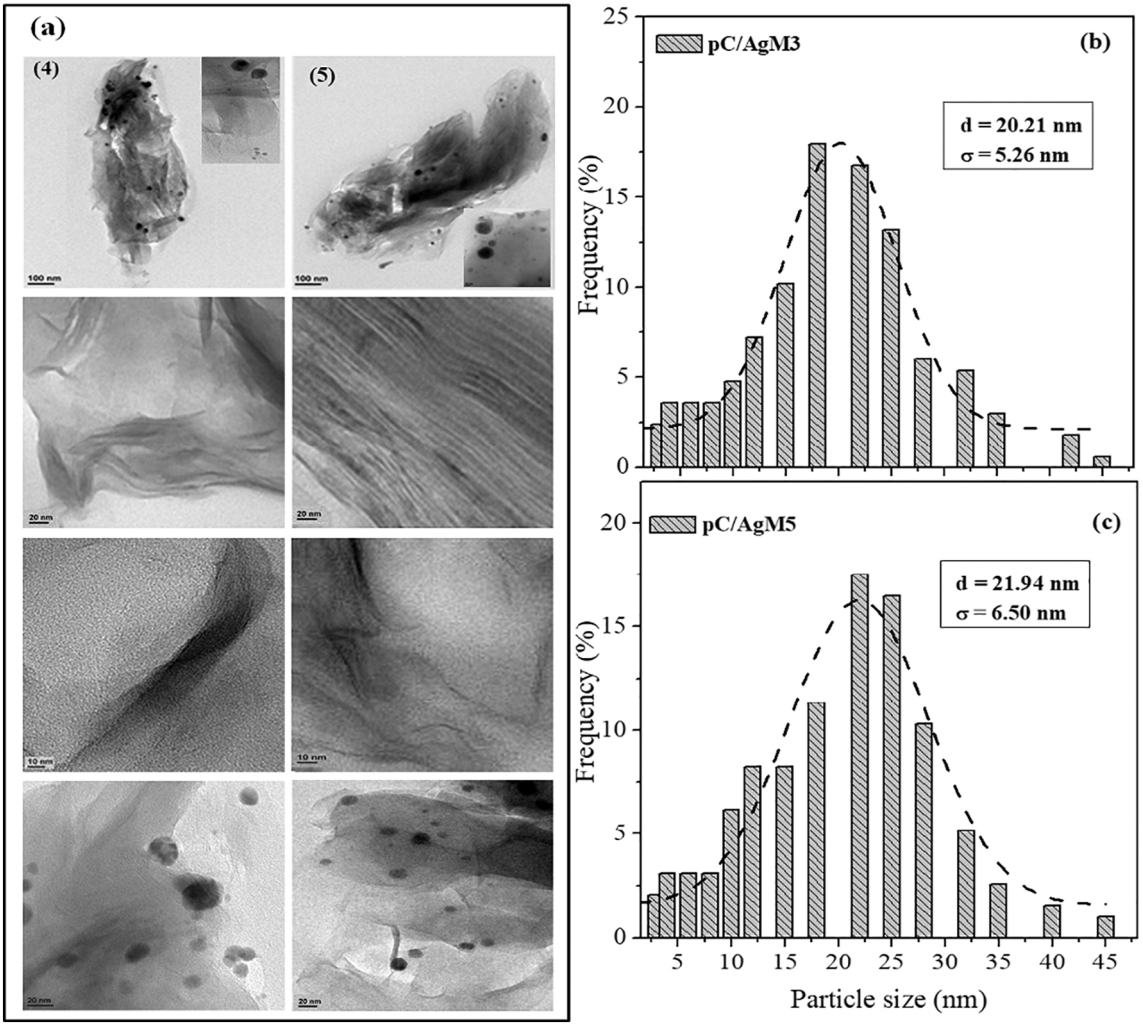
(a)
(4)
(5)
100 nm
100 nm
20 nm
20 nm
10 nm
10 nm
20 nm
20 nm
pC/AgM3
(b)
d = 20.21 nm
σ = 5.26 nm
Frequency (%)
pC/AgM5
(c)
d = 21.94 nm
σ = 6.50 nm
Frequency (%)
Particle size (nm)

Figure 7

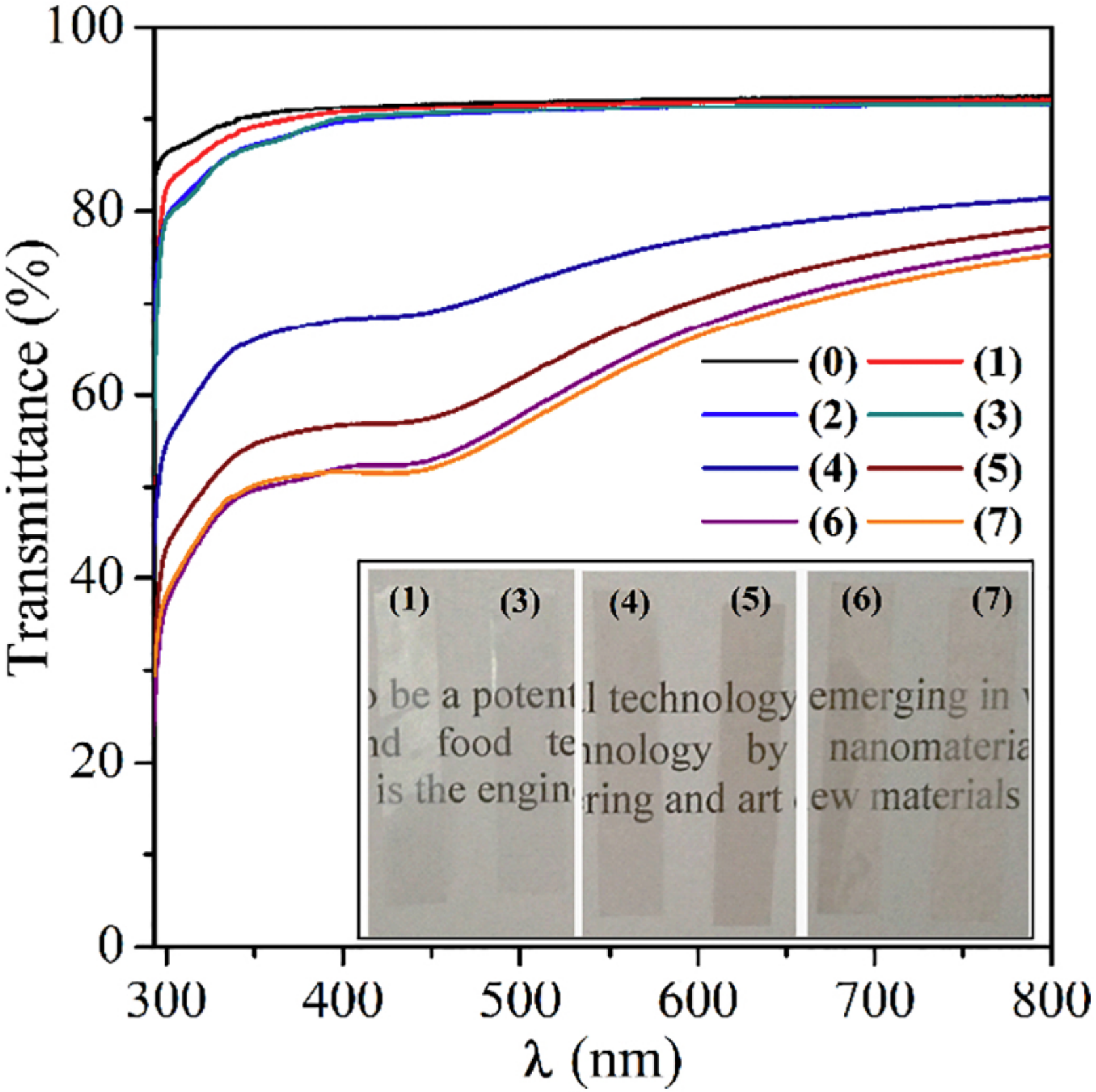
100
80
60
40
20
0
Transmittance (%)
300
400
500
600
700
800
λ (nm)
(0)
(1)
(2)
(3)
(4)
(5)
(6)
(7)
(1)
(3)
(4)
(5)
(6)
(7)

Figure 8

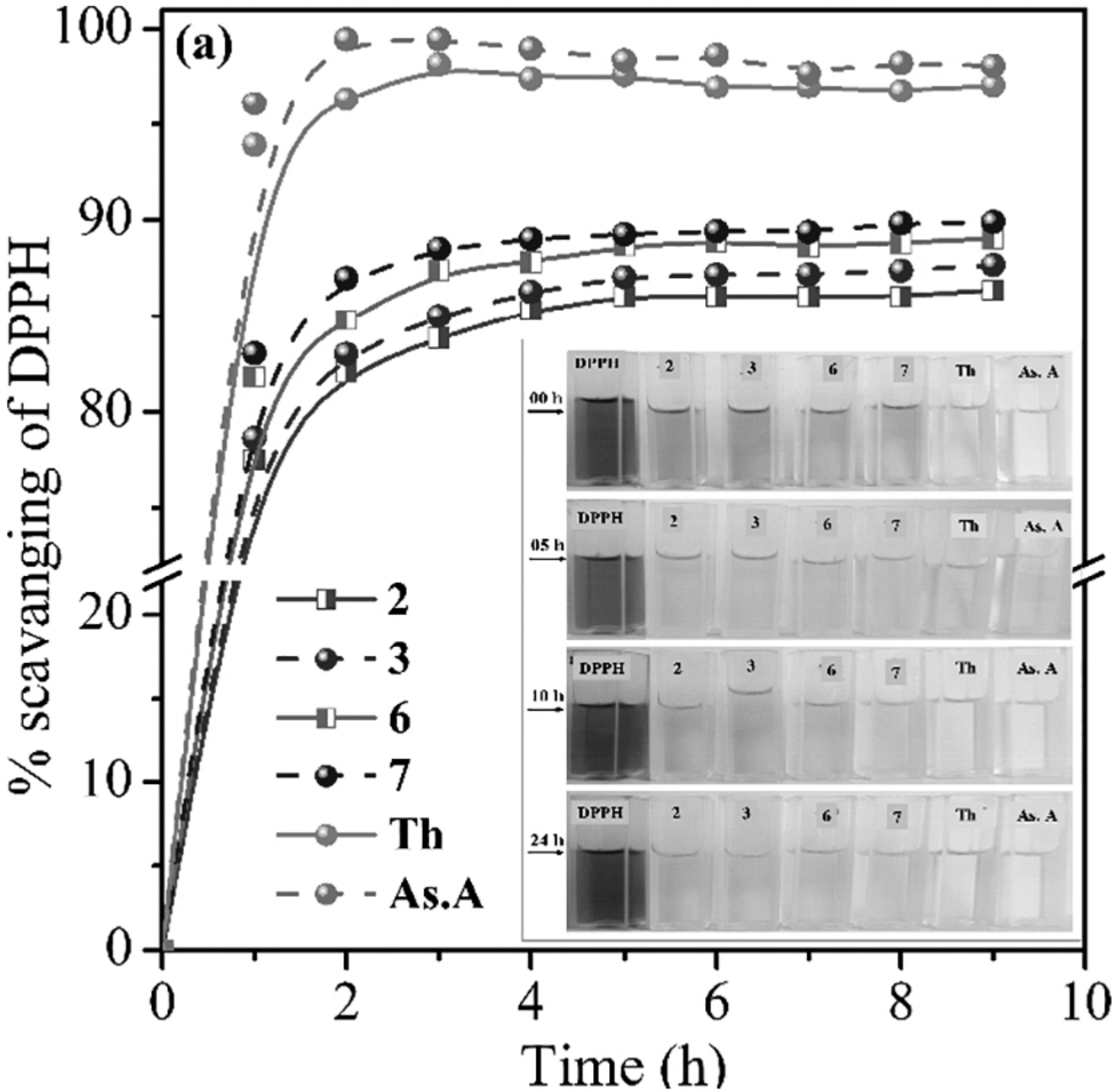
(a)
% scavanging of DPPH
Time (h)
0
10
20
80
90
100
0
2
4
6
8
10
2
3
6
7
Th
As.A
DPPH
00 h
05 h
10 h
24 h

Figure 9

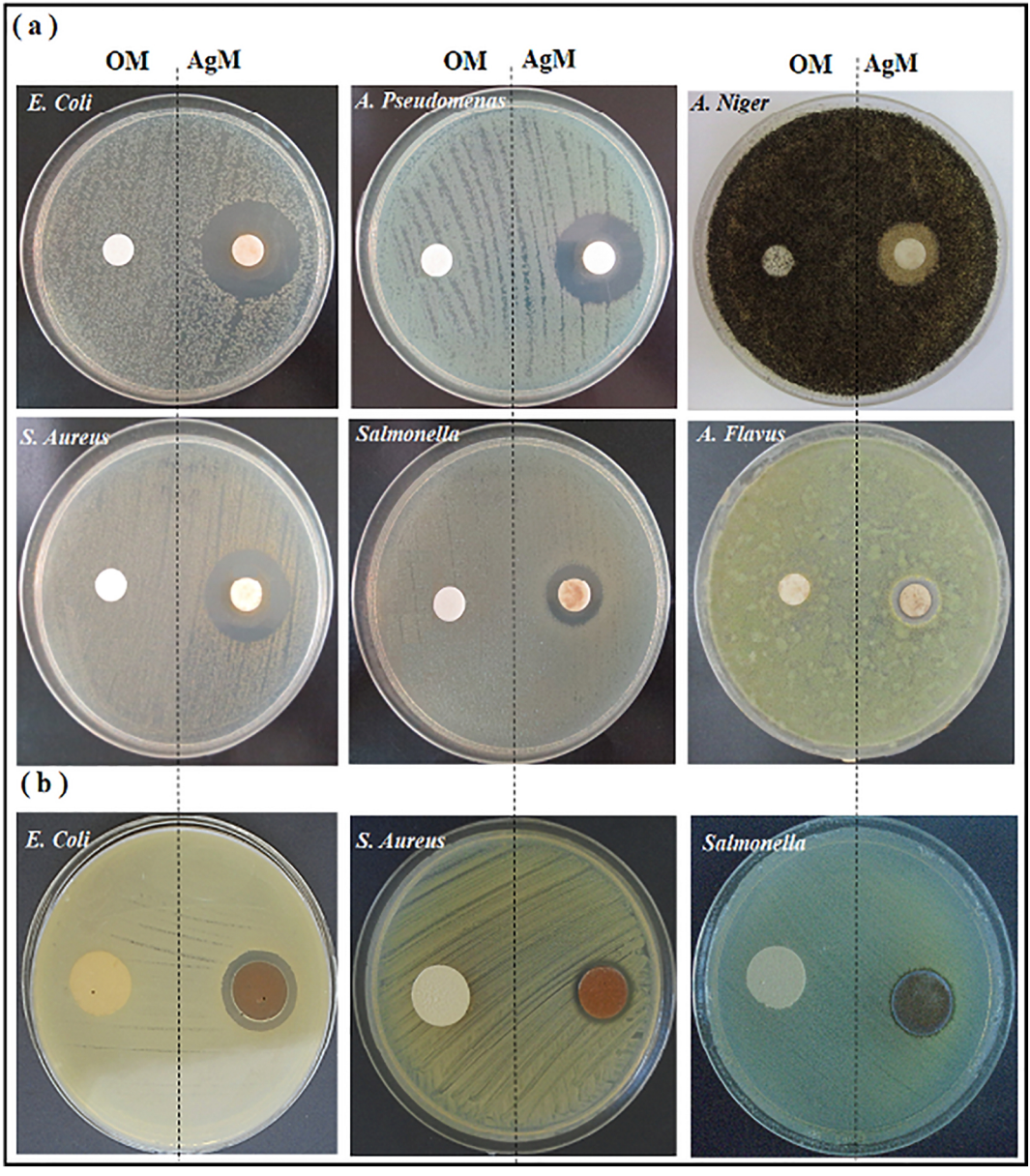
(a)
OM
AgM
OM
AgM
OM
AgM
E. Coli
A. Pseudomenas
A. Niger
S. Aureus
Salmonella
A. Flavus
(b)
E. Coli
S. Aureus
Salmonella

Figure 10

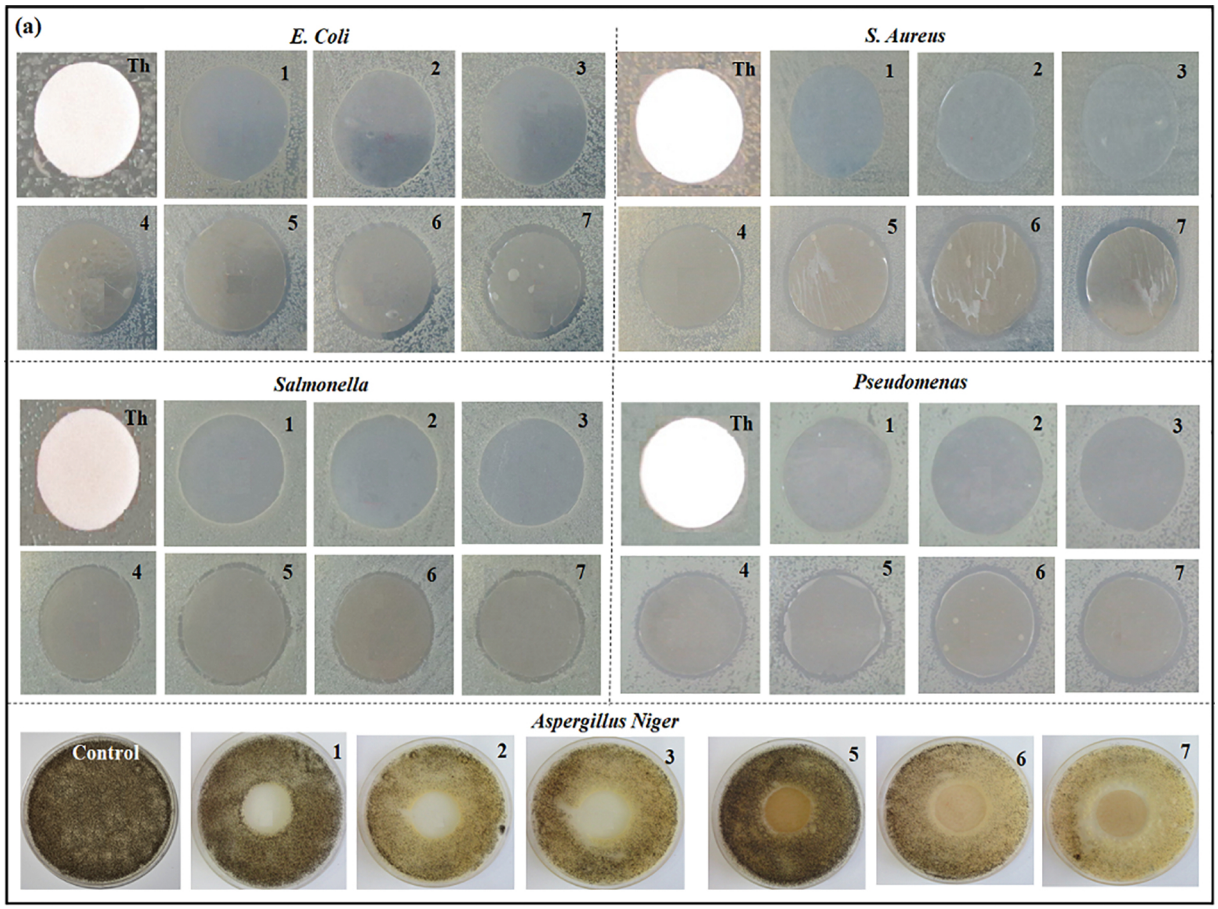
(a)
E. Coli
Th
1
2
3
4
5
6
7
S. Aureus
Th
1
2
3
4
5
6
7
Salmonella
Th
1
2
3
4
5
6
7
Pseudomenas
Th
1
2
3
4
5
6
7
Aspergillus Niger
Control
1
2
3
5
6
7

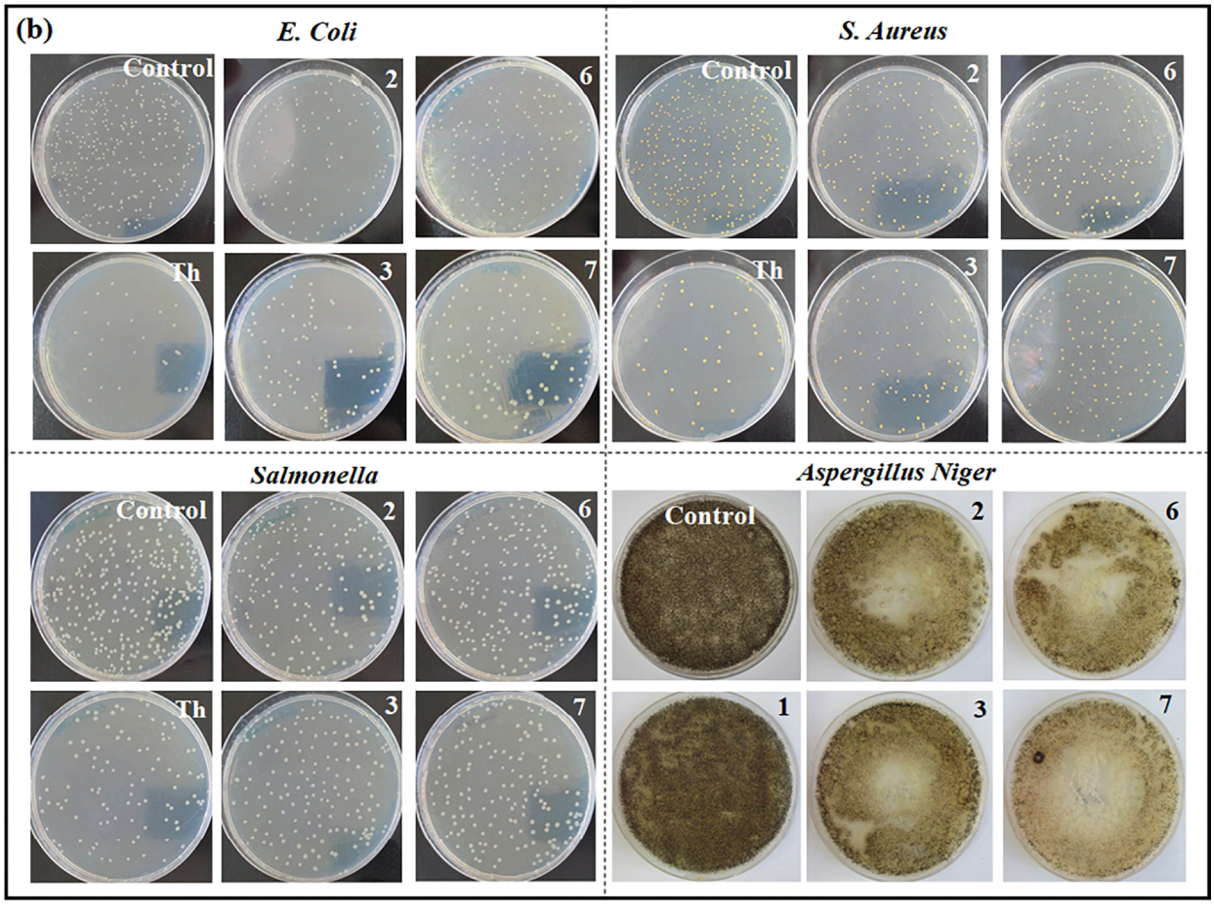
(b)
E. Coli
Control
2
6
Th
3
7
S. Aureus
Control
2
6
Th
3
7
Salmonella
Control
2
6
Th
3
7
Aspergillus Niger
Control
2
6
1
3
7

Figure 11

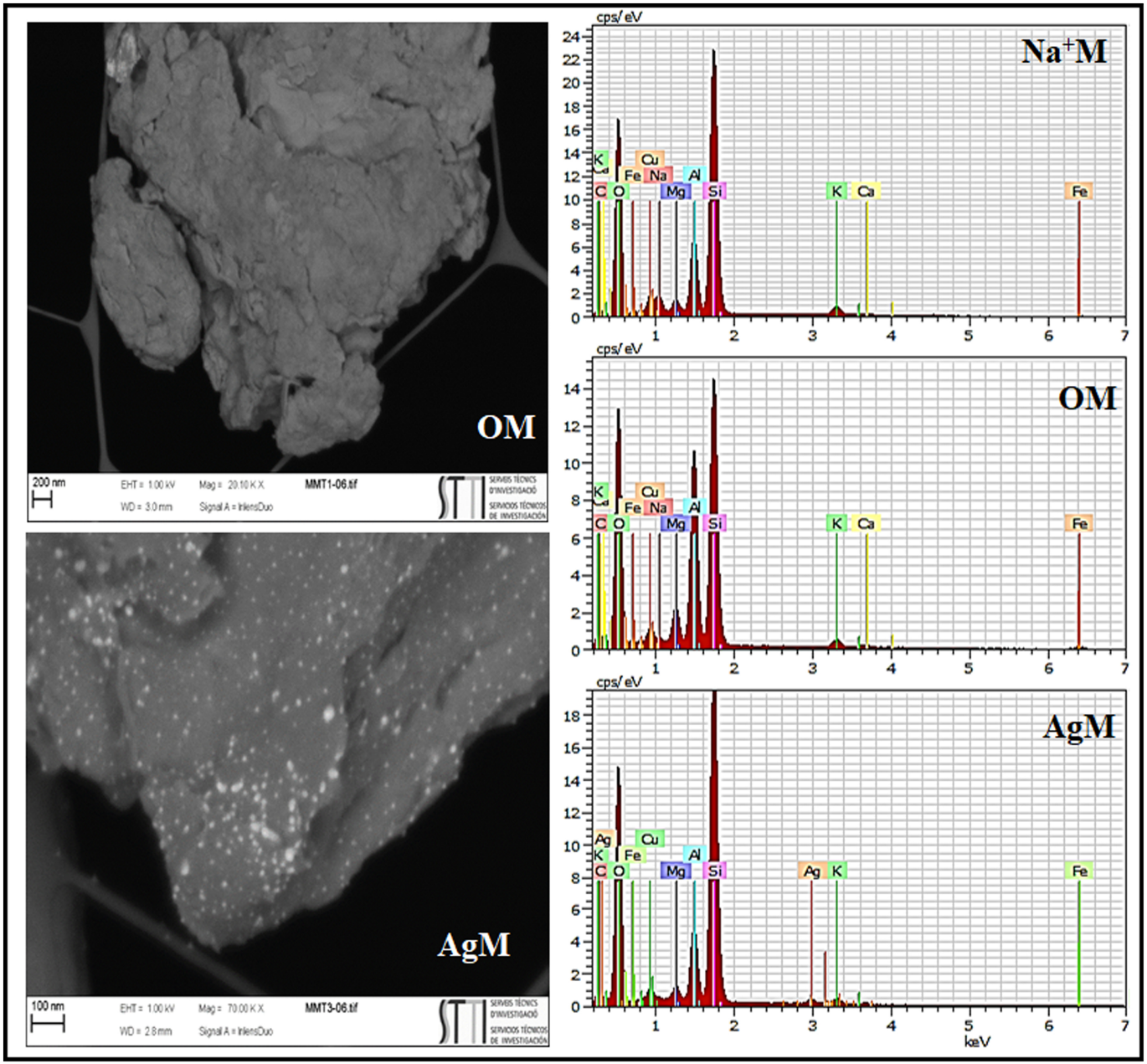
OM
200 nm
EHT = 1.00 kV
WD = 3.0 mm
Mag = 20.10 K X
Signal A = InlensDuo
MMT1-06.tif
AgM
100 nm
EHT = 1.00 kV
WD = 2.8 mm
Mag = 70.00 K X
Signal A = InlensDuo
MMT3-06.tif
cps/eV
Na+M
OM
AgM
C O Mg Si K Ca Fe
Fe Na Al Cu
Ag
keV

Figure 12

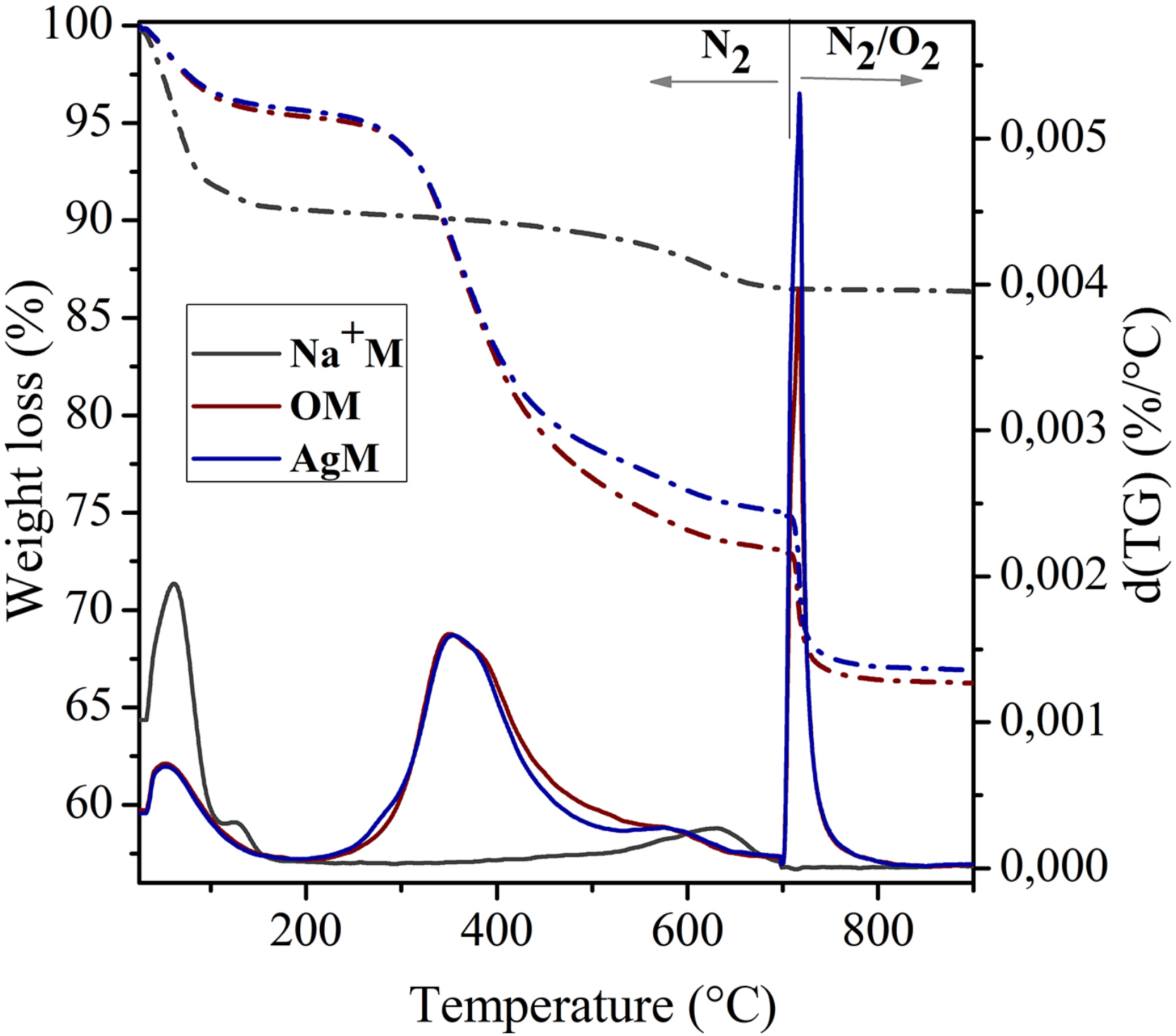
100
95
90
85
80
75
70
65
60
Weight loss (%)
N_2
N_2/O_2
Na^+M
OM
AgM
0,005
0,004
0,003
0,002
0,001
0,000
d(TG) (%/°C)
200
400
600
800
Temperature (°C)

Figure 13

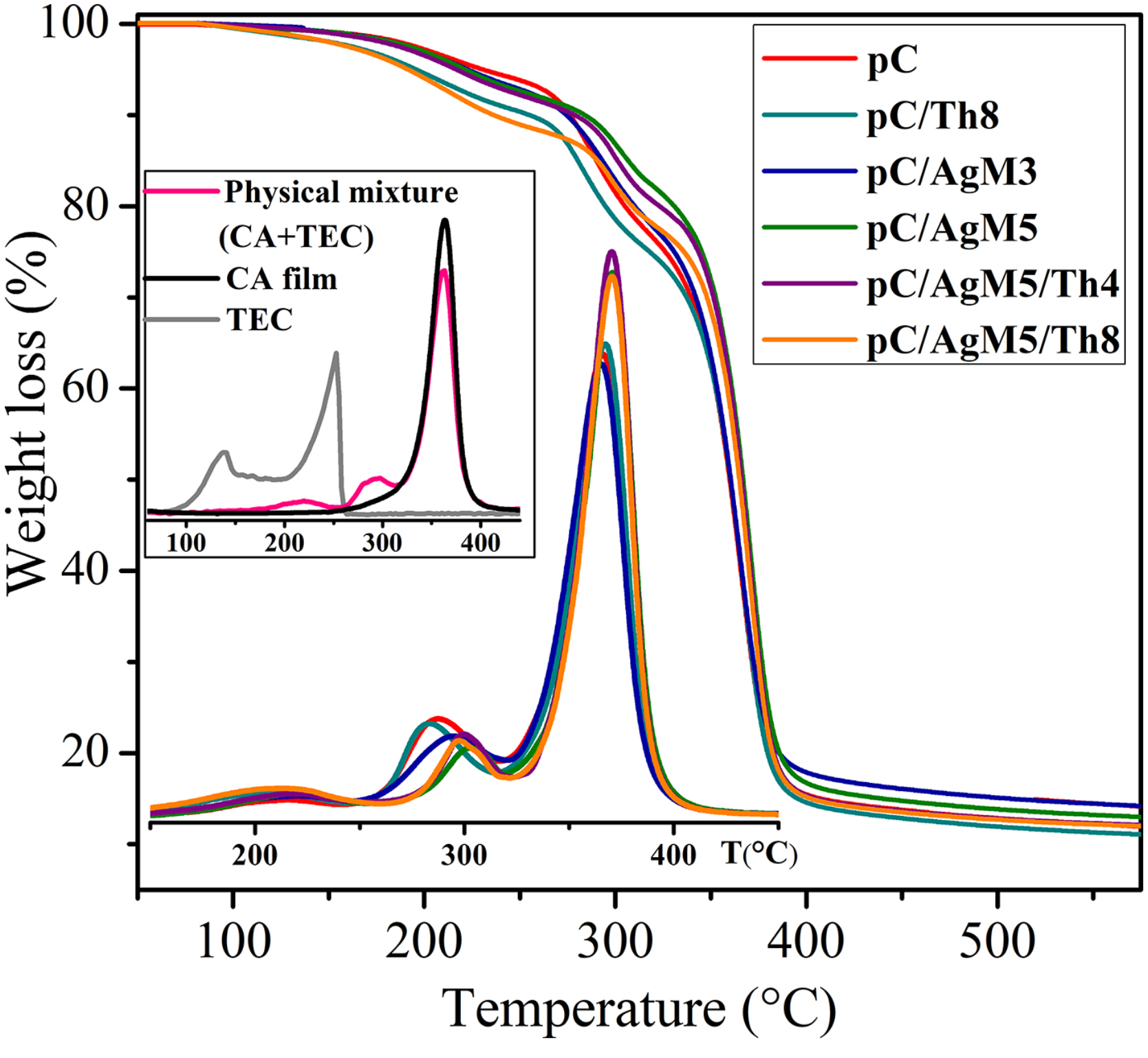
Weight loss (%)
Temperature (°C)
pC
pC/Th8
pC/AgM3
pC/AgM5
pC/AgM5/Th4
pC/AgM5/Th8
Physical mixture (CA+TEC)
CA film
TEC
T(°C)

Figure 14